A STUDY OF ARTIFICIAL METEORS AS ABLATORS

By Charles E. Shepard,* John W. Vorreiter,*
Howard A. Stine,* and Warren Winovich*

Ames Research Center, NASA
Moffett Field, California

SUMMARY

Photographic observations of meteors could provide more reliable information on the meteoroid hazard to space travel if meteor ablation and radiation phenomena were better understood.

Static tests in an ultrahigh-enthalpy plasma jet reveal that artificial meteors of gabbro or basalt ablate and radiate similarly to samples cut from natural stone meteorites. Likewise, steel specimens duplicate the behavior of natural iron meteorite material. During ablation the comparable materials grow in frontal area, decrease in average density, and emit light in the same manner.

SYMBOLS

A	test body frontal area, m^2
A_o	initial test body frontal area, m^2
C_D	drag coefficient, dimensionless
C_H	heat-transfer coefficient, dimensionless
g	acceleration of gravity, m sec^{-2}
H_{AV}	mass average total enthalpy, J kg^{-1}
I	luminous intensity normalized to 100 km distance, W m^{-2}
$I_{gas\ cap}$	gas-cap luminous intensity normalized to 100 km, W m^{-2}

99

*Research Scientist

L	model length, m
L_o	initial model length, m
m	body mass, kg
Q^*	effective heat of ablation, J kg^{-1}
$\dot{Q}_o$	model cold-wall heating rate, W
$\dot{Q}_{rad}$	model radiative power, W
$\dot{q}_o$	cold-wall stagnation-point heat-transfer rate, W m^{-2}
$\dot{q}_{o\ calc}$	calculated stagnation-point heat-transfer rate, W m^{-2}
$\dot{q}_{o\ meas}$	measured stagnation-point heat-transfer rate, W m^{-2}
$\dot{q}_{rad}$	radiative stagnation-point heat-transfer rate, W m^{-2}
r	radius, m
r_j	maximum jet radius, m
t	time, sec
V	velocity, m sec^{-1}
V_{eff}	effective velocity, m sec^{-1}
z	zenith angle measured from vertical, radian
α	thermal diffusivity, m^2 sec^{-1}
ρ	atmospheric density, kg m^{-3}
ρ_{eff}	effective atmospheric density, kg m^{-3}
ρ_m	test body density, kg m^{-3}
τ_o	luminous efficiency factor, W $sec^4 kg^{-1} m^{-5}$

INTRODUCTION

Although meteoric phenomena have been systematically studied for many years, world-wide interest in space travel has engendered new emphasis in the subject. In addition to the hazards they add to space travel [1], meteors provide examples of bodies in hypervelocity atmospheric entry and are,

therefore, of intrinsic interest to aerodynamicists [2,3]. A more basic reason for the study of meteoroids and meteorites rests in the clues they may furnish as to the origin of the solar system.

The primary knowledge of interplanetary debris stems from observations of meteors and examinations of the world's collections of meteorites. In spite of many difficulties, a considerable store of information has been obtained by astronomers during the past several decades. Photographs from two or more cameras with rotating shutters have provided sufficient information to determine the velocity, altitude, brightness, and angle of entry for meteors ranging in mass down to about 10^{-4} grams [4]. Smaller meteors can be detected by means of their radar echoes [5].

Although the random nature of meteors makes a systematic study difficult, the number flux of meteoroids in the vicinity of the earth has been determined as a function of estimated mass, as is shown on Fig. 1. The curve illustrated is divided into three major regions -- namely: that containing numerous dust particles or micrometeoroids; a middle region populated by cometary meteors and including the particle masses between 10^{-4} and 10^{0} grams that offer the greatest hazard to space travel; and, finally, a region of low flux populated by large asteroidal meteoroids. The curve is approximate because there is no precise way of determining the initial masses, especially of those meteors that do not survive entry. More important is the fact that meteor composition, density, and size are no better known than meteor mass. There is some evidence that the many small meteors which do not survive entry are mainly of cometary origin and may consist largely of ice [6].

Even though the composition of meteors for the mass range of primary interest, that is, between 10^{-4} and 10^{0} grams, is largely unknown, it proves to be of value to study the problem of meteor flight in a ground-based facility where specimens having compositions similar to those of known meteorites can be

subjected to the environment of an actual meteor entry. The purpose of this paper is to present the results of experiments designed to study the drag, ablation, and radiation behavior of meteor models in simulated atmospheric entry. A complete knowledge of such behavior would hopefully allow more precise estimates, such as that in Fig. 1, to be prepared.

ANALYSES OF METEORS

Typical Meteor Trails

The trajectories of meteors that have been photographed by the Super-Schmidt cameras [7] allow delineation of typical velocity and altitude ranges. Fig. 2 shows such trajectories of a number of meteors and includes one that is believed to be of asteroidal origin. These trajectories were selected at random from several hundred photographed in New Mexico, U. S. A. [8]. They cover an altitude range between 110 and 60 km with the majority terminating above 70 km. Although the speeds vary from about 11 to 70 km/sec, most are in the 15 to 30 km/sec range. However, for any given meteor, the observed portion of the entry occurs at very nearly constant velocity.

From the momentum equation taken in the flight direction:

$$m \frac{dV}{dt} = - \frac{1}{2} C_D \rho V^2 A + mg \cos z \tag{1}$$

The ballistic parameter, $m/C_D A$, can be derived:

$$\frac{m}{C_D A} = \frac{-(1/2)\rho V^2}{(dV/dt) - g \cos z} \tag{2}$$

From Eq. (2), curves of the ballistic parameter as functions of altitude for the meteor trajectories of Fig. 2 can be determined. They are presented in Fig. 3. No assumptions need be made as to meteor size, shape, density, or composition, nor need there be any restrictions on body rotation. If the drag coefficient remains roughly constant, it might be expected that the ballistic

parameter would decrease with decreasing altitude, because the factor m/A is roughly proportional to radius, and radius should decrease as ablation proceeds. Although many m/C_DA indeed decrease monotonically with altitude there are many that apparently do not, and in fact some exhibit increasing values of m/C_DA with decreasing altitude. Fig. 3 thus demonstrates that anomalies can be expected, and that a single meteor trail is not necessarily typical of others of the same mass that might enter on an identical initial trajectory.

Various theories have been advanced to explain the deviations in ballistic parameter from the behavior that would be expected. "Fragmentation" has been proposed to explain the observation that m/C_DA can decrease more rapidly than it can be computed [7]. On the other hand, one explanation advanced for the anomalous increases observed for m/C_DA may be found in the rotational behavior of an asymmetrical body. Although a low-drag attitude is not aerodynamically stable, several gyrations might occur before sufficient damping locks the body into a high-drag attitude. Once the body is in the high-drag attitude, however, its drag should be nearly identical with that of a sphere of the same mass.

A number of arc-jet ablation tests have shown that in a low-density flow environment the melt of many materials tends to foam as it runs rearward and solidifies, with a simultaneous decrease in average density and increase in frontal area. Subsequently, the foamed material often breaks away to produce a sudden increase in the ballistic parameter, m/C_DA. This phenomenon, which will be discussed in greater detail in a later section, can account both for the observation that m/C_DA can decrease more rapidly than would be expected and that m/C_DA can increase abruptly.

Methods of Meteor Analysis

Two methods of analyzing meteor data in principle allow determination of the mass and density. In applying either method it is usually assumed that the

body retains a spherical shape, that its average density is constant during entry, and that it either loses mass at a rate [9]

$$\frac{dm}{dt} = -\frac{1}{2}\frac{C_H A \rho V^3}{Q^*} \tag{3}$$

or alternatively the mass loss rate is related to the luminous intensity, I, according to the formula [10,11]:

$$\frac{dm}{dt} = \frac{-2I}{\tau_o V^3} \tag{4}$$

where τ_o, the luminous efficiency factor, is usually assumed to be constant and the mass lost is assumed to be completely vaporized. In the dynamical method, Eqs. (1) and (3) would completely describe the meteor in terms of mass and density if the drag coefficient, heat-transfer coefficient, and effective heat of ablation were all known. In the photometric method, Eqs. (1) and (4) would allow mass and density determinations if τ_o, the luminous efficiency factor, were accurately known. Unfortunately, there are large uncertainties in the knowledge both of the luminous efficiency factor and of the effective heat of ablation, although drag coefficient and heat-transfer coefficient can be estimated with sufficient precision.

In a series of papers [9,12,13], Allen and others discussed the above methods and how they could be improved to give better estimates of meteor mass and density. It was concluded that the dynamical method (Eq. (3)) was satisfactory for asteroidal meteors [13], whereas the photometric method (Eq. (4)) was superior for the smaller and faster cometary meteors [13]. In applying the dynamical method, it was suggested that the power radiated from the body be subtracted from the power absorbed by the body so that Eq. (3) would read

$$\frac{dm}{dt} = -\frac{(1/2)C_H A \rho V^3 - \dot{Q}_{rad}}{Q^*} \tag{5}$$

and that the drag contribution of ablating vapors be considered in Eq. (1). In the photometric method, it was recommended that the gas-cap radiation be

subtracted when the luminous efficiency factor was determined:

$$\frac{dm}{dt} = - \frac{I - I_{gas\ cap}}{(1/2)\tau_o V^3} \tag{6}$$

For the purposes of this paper, Eqs. (5) and (6) constitute the defining equations for experimentally evaluating effective heat of ablation Q^* and luminous efficiency factor, τ_o.

EXPERIMENTAL PROGRAM

A number of materials having compositions thought to be typical of meteors were tested to determine their effective heats of ablation and luminous efficiency factors. These values were then compared with calculated values and those commonly used in meteor analysis. In addition, the melting, the foaming of the melt, and the behavior of the liquid run-off were examined to determine their effects on frontal area, apparent density, and mass loss rate. All tests were conducted in air in constricted-arc supersonic jet apparatus [14].

Constricted-Arc Apparatus

Basically, a constricted-arc plasma jet is a combination of a cascade arc and a DeLaval nozzle as shown in Fig. 4. The cathode, protected against oxidation by a small argon flow, is located at the upstream end, and a multiple-element anode is located in the divergent section of the supersonic nozzle. A direct-current electric arc is maintained between the electrodes. Air from a pressurized reservoir is introduced into the constrictor. The air is heated as it passes near the arc, becomes conducting and eventually becomes a part of the arc core. With the arrangement shown, the gas is maintained at a high temperature even as it passes through the supersonic portion of the nozzle. The average energy content of the stream can be determined by subtracting the power lost to the water-cooled components from the electrical energy supplied to the

arc. The average total enthalpy is obtained by dividing the net power in the stream by the air flow rate. The average enthalpy, the flow rate, and the nozzle expansion ratio govern the test section impact pressure.

The two constricted-arc supersonic jets employed in the investigation differ primarily in size. The larger of the two has a throat diameter of 2.54 cm and a nozzle exit diameter of 46 cm, and operates at gross powers up to 5 MW. The smaller has a throat diameter of 1.27 cm, a nozzle exit diameter of 6 cm, and absorbs up to 1 MW. Photographs of the two pieces of apparatus are shown in Figs. 5(a) and 5(b).

The performance map in Fig. 6 relates to the constricted-arc supersonic jets used in the artificial meteor tests. It shows the operating ranges in terms of achievable average total enthalpy as a function of test section impact pressure. The points labeled A through E correspond to conditions at which meteor ablation behavior was studied. Typical radial flow profiles of pressure and stagnation-point heat-transfer rate at the jet exit of the larger unit are shown in Fig. 7. A region near the axis of symmetry has relatively uniform flow at known conditions.

Simulation of Meteor Entry With Constricted-Arc Apparatus

To simulate meteor entry, velocities from 11 to 70 km/sec of cold gas are desired, with a density range corresponding to that at altitudes from about 60 to 110 km. Unfortunately, it is not possible to duplicate such flows exactly by rapid expansion of a hot gas through a nozzle. As is well known, the thermochemical rate processes do not keep pace with the rapid volume increase, and not all of the available energy is converted to kinetic energy. A flow of relatively hot gas having an excess of excited species is produced that moves at reduced velocity. However, it is possible to measure the heating rates expected during meteor entry by exposing a metallic calorimeter to the flow

at the proper total enthalpy and at the proper impact pressure. Furthermore, an "effective" velocity can be defined as the square root of twice the total enthalpy at the core, and an "effective" altitude can be defined in terms of an "effective" density. Effective density is determined from the quotient of impact pressure, ρV^2, and the square of the "effective" velocity. Performance of constricted-arc apparatus is shown in Fig. 8 in terms of effective velocity and effective altitude. Superimposed is the region of velocities and altitude which are of interest in studies of meteors. This figure shows that the low-velocity, high-altitude region of meteor entry can be covered by the 2.54-cm-diameter constricted-arc apparatus, and that somewhat lower effective altitudes can be reached with the smaller equipment. Again, the points labeled A through E correspond to conditions at which meteor ablation behavior was studied.

For the simulation of asteroidal meteors, a series of stone and steel test bodies were prepared. Their shapes and dimensions are given in Fig. 9. The nose radius was selected to minimize shape changes under ablating conditions. The igneous materials basalt and gabbro were selected as being representative of natural chondrites. A low carbon steel was selected as being representative of natural iron meteors. In addition to the artificial meteors, a number of specimens were prepared from a 1 kg specimen of the Plainview, Texas, veined intermediate chondrite and from a 1.3 kg Canyon Diablo, Arizona, coarse octahedrite iron meteorite. The densities and compositions of the meteor test bodies are listed in table I.

The ballistic parameters, m/C_DA, of the test bodies ranged from about 30 kg/m^2 for the stones to about 100 kg/m^2 for the steel and iron meteorite models. Although these values are larger than would be appropriate for the altitude range of interest, as shown in Fig. 3, the large size permits more accurate measurements of recession rates and flange growth phenomena than would otherwise be possible. As a result, the tests are conducted at an altitude

that is too high and a heating rate that is too low for typical meteors of the same m/C_DA. Whereas typical meteors burn up in about 1 second, the arc-jet tests extend from 3 seconds to about 2 minutes. Further, the quasi-steady-state tests do not simulate transient heating behavior of a meteor on a plunging trajectory because density and velocity do not vary with time.

An ablating meteor ejects either molten material or vapor, depending upon the relative magnitude of the shear and deceleration forces that tend to tear the body apart, and the surface tension and viscosity forces that tend to hold it together. Although the plasma jet tests generate the proper magnitude of shear force, surface tension, and viscosity, the deceleration force is absent. As a result there is no inertial force to balance the drag, and fluid particles of the artificial meteor experience larger net forces than those of actual meteors. This problem is discussed by Chapman [15] in a similar study involving the ablation of tektites. Tests were made in a vertical jet in which the dynamic force opposed the force of gravity. Under conditions approximating free flight, larger flanges were generated than could otherwise be produced. Unfortunately it was not possible to balance these forces with the present apparatus; consequently one would expect larger loss of molten material than would occur in the corresponding free-flight case.

Also, liquid runoff complicates the measurement of luminosity in the plasma jet tests. For, whereas light from vaporizing fragments that may trail from actual meteors contributes to the observed luminosity, melted material from artificial meteors did not remain in view of the optical equipment and thus could not contribute to the observed light output.

Instrumentation and Test Procedure

The plasma-jet apparatus (Fig. 5) was instrumented to measure the recession rate, the approximate frontal area, mass loss, and luminosity of the meteor

models at known stream conditions. Total enthalpy and impact-pressure measurements permitted an effective velocity and an effective altitude to be defined. Nickel-plated copper calorimeters of the same size and shape as the meteor models yielded the cold-wall stagnation-point heat-transfer rates.

Motion picture cameras measured the rate at which the nose of the model receded, the rate at which the frontal area increased, and provided a visual record of each run. The motion picture coverage was augmented by still photographs both in black and white and in color. Luminosity was measured by a light meter having a spectral response similar to that of the human eye since meteor luminous efficiencies are often referred to a visual spectral sensitivity. Although the radiation from the test bodies was very intense, it was necessary to restrict the field of view of the light meter to a small area surrounding each model to minimize errors due to background radiation from the plasma stream. However, photographs of ablating bodies indicate that most of the light emanates from a volume having dimensions of a few body diameters, since melted material quickly blows away. Therefore, fields of view of about 8 by 13 cm and 15 by 30 cm were established by means of appropriate collimation for the constricted-arc jets of Figs. 5(a) and 5(b), respectively.

A scanning monochrometer, shown in Fig. 10, measured spectral radiation over a 0.35 to 0.70 micron wavelength band for the 98.5 and 91 km altitude test conditions. In addition to wavelength scanning, provisions were made to monitor radiation at various axial locations along the model in the free stream.

The test bodies of stone and iron were exposed to the arc-jet streams at conditions designated in table II. Test point (A) is a condition characterized by relatively high altitude and high effective velocity that yielded a relatively low-heat-transfer rate. Test points (B), (C), and (D) simulate flight at an altitude of about 91 km but at various increasing values of effective velocity, while test point (E) simulates flight at an altitude of 72.5 km.

Table III is a test schedule that lists the runs and includes information on model material, test condition, and initial and final masses of the test bodies.

RESULTS AND DISCUSSION

As a result of the plasma-jet tests at controlled conditions of velocity and enthalpy, several statements can be made regarding the ablation behavior of meteors. First, all of the specimens "foamed." That is, each built up a flange of relatively low-density, slag-like material that substantially increased the area exposed to the flow.

Although the stones grew most in frontal area, even the steel and iron meteorite materials more than doubled their frontal areas as is illustrated by the photographs of Fig. 11. Such behavior indicates that flange formation may be an essential process in the flight of stone and iron meteors, and is also known to be true of glassy meteors, the tektites [15]. Indeed, it was found impossible to measure a vaporization rate, because the slaggy material which built up was shed intermittently in relatively large chunks.

A second important result was the discovery that steel bodies behave in a manner like those made of natural iron meteorite. Similarly, the igneous rock gabbro exhibited ablation characteristics almost identical to those of natural stone meteorites.

The cooled foams recovered from the steel and terrestrial stone materials were similar to those recovered from the iron and stone meteorites, respectively. As shown in table IV, comparable materials had about the same density ratio of foam to virgin material and exhibited about the same decrease in foam density with increasing heating rate. Therefore, tests with easily obtainable terrestrial material can be expected to yield results characteristic of natural stone and iron meteors.

Another noteworthy characteristic of the meteor ablation was a striking difference between the behavior of stone and iron. Whereas both meteoritic

and terrestrial stone surfaces melt almost immediately upon entry into the high-temperature stream, and start foaming in a rather irregular manner, both meteoric iron and steel require a long time to reach melting temperature, after which a flange of material builds up in a regular way. Ultimately the melt blows away so that an abrupt change in mass occurs. Thus, for the altitude and velocity range covered by the tests, heat storage is an important mechanism for the iron and steel bodies.

Although the iron and stone models both lost mass at a more rapid rate near the end of the tests as large blobs of froth blew away, the tests revealed that iron and steel specimens also lose mass by an eruptive mechanism. As the ferrous models became incandescent, small particles were ejected from the main body with appreciable velocity and left luminous trails. Debris recovered from the vacuum system yielded, in addition to relatively large pieces of melted stone and iron, small magnetic spheroids that ranged in diameter from submicron to millimeter sizes.

Frontal Area

Curves of the area presented to the flow as a function of time are plotted in Fig. 12(a) for steel meteor models at test conditions (A) through (E). For test point (A) the models were very nearly in radiation equilibrium, and therefore exhibited a very small change in frontal area. However, at the 91 km altitude test points the projected areas increased by a factor of about 2-1/2 during the course of the runs, whereas at the relatively high heat flux of condition (E) the model frontal area nearly doubled. The principal difference between the five curves is the time required to start forming the flange.

In Fig. 12(b), five corresponding curves for the natural stone meteorite models are shown. Notice here that the flange starts to form almost immediately, that a somewhat larger increase in area is generally experienced, that the rate

of growth with time is about the same as for iron, and that the build up in area may be followed by an abrupt decrease. At the 72.5 km altitude, test condition (E), a flange of smaller area was produced that built up and broke off at many times the frequency of those for the high altitude test conditions.

The similar flange growth behavior of steel and natural iron meteorite is shown in Fig. 12(c). That of gabbro and basalt stone and natural stone meteorite is evident in Fig. 12(d), where foaming the behavior of the gabbro approximately matches that of the Plainview chondrite.

Recession Rate

Curves of material recession rates of the meteor models for various flow conditions are illustrated in Fig. 13. The rates at which the steel models ablated are shown in Fig. 13(a). Notice that at high altitude and high velocity practically no material was lost. For conditions (B), (C), and (D), the face of the model recedes at an increasing rate with increasing velocity, whereas the time interval required for the recession to start decreases. The time lag at condition (E) is almost negligible. The results for the stone models are shown on Fig. 13(b). The results are similar to those for the steel model; however, little time lag occurs in establishing recession. At 72.5 km altitude the model face recedes more rapidly than at higher altitudes and fluctuates in apparent length as the material melts and boils violently. Again, good agreement is found between the steel model and the iron meteorite in Fig. 13(c) and between the gabbro, basalt, and stone meteorite models in Fig. 13(d). At test point (E), the specimens melted and were completely blown away in 11 seconds or less as compared to typical melting times of 60 seconds at the 91 km simulated altitude.

Effective Heats of Ablation

A value of effective heat of ablation, based on stagnation-point heat-transfer rate, can be determined experimentally by means of Eq. (5) if the heat input is taken from the cold-wall stagnation-point calorimeter measurements listed in table II. When this is done, the following expression for effective heat of ablation is obtained:

$$Q^* = \frac{\dot{q}_{o,\ meas} - \dot{q}_{rad}}{\rho_m\ dL/dt} \tag{7}$$

Here $\dot{q}_{rad}$ is the power per unit area that the incandescent model face radiates to its surroundings. Because a large part of the radiation loss occurred in the infrared, to which the luminosity meter was not sensitive, an approximate correction for radiation was determined from the brightness temperature of the melting surface material observed during each test. It was found that the brightness temperature of the liquid melt was approximately constant, and was approximately equal to the melting temperature of the material. The magnitude of the radiation correction varied from about 40 percent for test condition (A) to less than 2 percent for test condition (E). Values of effective heats of ablation so determined are shown in Fig. 14 as a function of the Fourier modulus, $\alpha t/L_0^2$. For small values of this dimensionless time parameter, corresponding to high heat-transfer-rate tests of low thermal diffusivity material, the effective heats of ablation approach the sum of the sensible heat required to raise the material from room temperature to vaporization temperature and the latent heats of fusion and vaporization. As the parameter $\alpha t/L_0^2$ increases, however, the heat stored in the unmelted portion of the body assumes an increasing influence, and Q^* decreases toward the latent heat of fusion.

Luminosity Measurements

The luminous intensities of gabbro, basalt, and stone meteorite models, as measured by a light meter with about the same spectral sensitivity as the human eye, are compared in Fig. 15(a). The intensities, when normalized to a distance of 100 km and plotted as a function of time, are observed to be of comparable magnitudes. Luminous intensities for the steel and iron meteorite models are also seen to be similar in Fig. 15(b) although the comparison is hampered by low levels of the light-meter signals. The stone meteor models were about 10 times brighter than the iron and steel models at 91 km altitude and about 3 times brighter at 72.5 km altitude.

Fig. 16 is a comparison of radiation spectra of steel and stone models and of the jet free stream. Spectrograms generated by the scanning monochrometer of Fig. 10 reveal the predominance of sodium D-line radiation of the terrestrial and meteoric stones. The iron and steel models radiate strongly in the blue and violet portion of the visible spectrum and the spectrogram of Fig. 16 shows that the magnitude of iron radiation is greater than that of stone in the 0.35 to 0.45 micron wavelength band.

The data presented are typical for altitudes of 91 and 98.5 km, but the spectra for the 72.5 km altitude tests were not recorded. In an earlier test, a spectrogram of basalt in nitrogen at a simulated altitude of about 70 km indicated strong iron radiation, although the sodium D-line was still prominent.

Motion pictures indicated that in the test runs, the bulk of material was lost when the melt layer blew off. When no material blew off, the model either lost a small amount of mass or, in two cases, gained slightly. Such mass gains are believed to be due to oxidation and/or nitriding reactions between melt layers and the plasma stream. It would have been possible in principle to collect all of the melted material, and by careful weighing and chemical analysis to determine the vaporization rate. Unfortunately, however, all of the

melted material could not be recovered. For these reasons the luminous efficiency factor as conventionally defined (Eq. (6)) could not be determined. Nevertheless, a luminous efficiency factor was calculated in terms of the total mass loss rate. This was accomplished by inserting measured values of total mass loss rate and total luminous intensity minus gas-cap radiation into Eq. (6), thereby evaluating τ_0. On the basis of the present tests, one can argue in justification of this procedure that large stone and iron meteors almost certainly lose mass primarily by liquid runoff and secondarily by vaporization. Although vaporization is certainly essential to the production of light, it must follow from and be a consequence of melting.

The resulting values of luminous efficiency factor for the various materials are plotted in Fig. 17 as a function of the Fourier modulus, $\alpha t/L_0^2$. Fourier modulus is a convenient correlating parameter for luminous efficiency factor measurements because heat storage, acting as an energy sink, will reduce luminosity. At values of $\alpha t/L_0^2$ less than about 0.03 the experimentally determined τ_0's are constant, whereas at about 0.3 the value of τ_0 has decreased by more than two orders of magnitude. Although these experimental data are undoubtedly too low because the total mass loss, rather than the vapor mass loss determined luminous efficiency factor, the agreement with values of τ_0 from Refs. 11, 16, and 17 is surprisingly good for small values of $\alpha t/L_0^2$. The reference values of τ_0 were corrected from "photographic" to "visual" luminous efficiency factor as recommended by Verniani [11].

CONCLUSIONS

Ablation tests in high-enthalpy plasma jets that in certain respects simulate the entry environment of meteors led to several conclusions about the ablation behavior of stone and iron. It was found that low carbon steel and igneous rock (gabbro and basalt) had ablation characteristics similar to those

of natural iron and stone meteorite materials. Therefore, ablation of asteroidal meteors can be studied by testing readily available terrestrial material.

Both stone and iron materials increase in frontal area during early stages of ablation, and form flanges of low-density slag that approximately double the frontal area. Such behavior results in a decrease in average density and in the ballistic parameter, m/C_DA. When these blobs of slag are shed abruptly, the ballistic parameter increases suddenly, and this phenomenon is proposed as an explanation of the fact that such anomalous behavior has been observed for some meteors. Because flanges form on steel and iron meteorite models, it is concluded that moisture apparently is not essential to foaming, although its presence undoubtedly contributes to the process.

For heavy bodies ablating at low air density very little mass is vaporized, perhaps because deceleration effects are not reproduced. Instead, heat soak, melting, and subsequent liquid runoff apparently absorb the majority of the incoming energy flux, possibly as a result of a mismatch between ballistic parameter and stream density. The relatively low values of effective heats of ablation determined from surface recession rates reflect this fact, especially in steel and iron meteorite models tested at low-heat-transfer rates when appreciable heat storage takes place. Conversely, when stone models are tested at high-heat-transfer rates which result in a relatively low Fourier modulus $\alpha t/L_0^2$, the measured values of effective heats of ablation, Q^*, approach those required to melt and vaporize the bodies completely.

Luminous intensity measurements indicate that the radiation characteristics of the igneous rocks basalt and gabbro closely match those of specimens cut from natural stone meteorites. Similarly, low carbon steel and natural iron meteorite exhibit closely matched luminous intensity characteristics. Over the simulated altitude and velocity range, the luminosity of the metal models is less than

that of the stone models. Although the corresponding luminous efficiency factors determined for the various materials are smaller than expected, the liquid runoff is greater during static tests in the plasma jet than it would be for actual meteoric entry where the inertial forces are large. Moreover, material blown away from the artificial meteor did not contribute to the luminosity measurement; whereas the light of the entire meteor trail is included in photographic determinations of luminous efficiency factor. Heat storage affected the luminosity measurements; consequently the Fourier modulus describing this effect correlated the luminous efficiency factor data for both iron and stone bodies.

Although there are many difficulties in establishing an experimental value, the luminous efficiency factor approaches a reasonable limit as heat storage effects decrease and mass loss by vaporization becomes important.

REFERENCES

1. Whipple, F. L.: "On Meteoroids and Penetration," J. Geophys. Res., 68, 4929-4939 (1963).
2. Riddell, F. R., and Winkler, H. B.: "Meteorites and Re-Entry of Space Vehicles at Meteor Velocities," ARS J., 32, 1523-1530 (1962).
3. Romig, M. F.: "Physics of Meteor Entry," AIAA J, 3, 385-394 (1965).
4. Whipple, F. L.: "Photographic Meteor Studies - I," Am. Philosophical Soc., 79, 499-548 (1938).
5. Lovell, A. C. B.: Meteor Astronomy, Oxford, Clarendon Press, 1954.
6. Whipple, F. L.: "A Comet Model. I. The Acceleration of Comet Encke." Astrophys. J., 111, 375-394 (1950).
7. Jacchia, L. G., Verniani, F., and Briggs, R. E.: "An Analysis of the Atmospheric Trajectories of 413 Precisely Reduced Photographic Meteors," SP No. 175, Smithsonian Instit. Astrophys. Obs., April 23, 1965.

8. Jacchia, L. G., and Whipple, F. L.: "Precision Orbits of 413 Photographic Meteors," 4, Smithsonian Contributions to Astrophysics, 97-129 (1961).

9. Allen, H. J., and James, N. A.: "Prospects for Obtaining Aerodynamic Heating Results From Analysis of Meteor Flight Data," NASA TN D-2069 (1964).

10. Öpik, E. J.: "Physics of Meteor Flight in the Atmosphere," Interscience Tracts on Physics and Astronomy, No. 6, Interscience Publishers, Inc., New York (1958).

11. Verniani, F.: "On the Luminous Efficiency of Meteors," Smithsonian Contributions to Astrophysics, 8, 141-172 (1965).

12. Allen, H. J., Baldwin, B. S., Jr., and James, N. A.: "Effect on Meteor Flight of Cooling by Radiation and Ablation," NASA TN D-2872, 1965.

13. Allen, H. J., and Yoshikawa, K. K.: "Luminosity From Large Meteoric Bodies," Presented at Meeting on Astronomy and Physics of Meteors sponsored by Smithsonian Astrophysical Observatory, Aug. 28-Sept. 1, 1961, Smithsonian Contributions to Astrophysics 7, 181-193 (1963).

14. Stine, H. A., Watson, V. R., and Shepard, C. E.: "Effect of Axial Flow on the Behavior of the Wall-Constricted Arc," In: AGARD. Arc Heaters and MHD Accelerators for Aerodynamic Purposes, pt. 1, 451-485 (1964) AGARDOGRAPH-84.

15. Chapman, D. R.: "On the Unity and Origin of the Australasian Tektites," Geochimica et Cosmochimica Acta 28, 841-880 (1964).

16. Cook, A. F., Jacchia, L. G., and McCrosky, R. E.: Luminous Efficiency of Iron and Stone Asteroidal Meteors. Proc. Symp. Astronomy and Physics of Meteors, Smithsonian Astrophysical Observatory, Cambridge, Mass., Aug. 28-Sept. 1, 1961, 209-220 (1963).

17. Jacchia, L. G.: "Ballistics of the Upper Atmosphere," Harvard Coll. Obs. and Center of Analysis. M.I.T. Tech. Rep. No. 2, Harvard Reprint Ser. II, 30 pp. (1948).

Table I.- Artificial Meteor Physical Characteristics

	Steel	Coarse octahedrite iron meteorite, Canyon Diablo, Arizona	Veined intermediate chondrite stone, Plainview, Texas	Basalt	Gabbro
Density, kg/m^3	7,780	7,800	3,590	2,830	2,920
Composition:					
Fe, percent	99+	89.7	17.23		
Ni		9.1	1.58		
C	.15				
SiO_2			36.52	48.2	48.2
MgO			23.48	7.51	7.51
FeO and FeO_3			8.87	9.11	9.11
Al_2O_3			2.43	17.9	17.9
CaO			1.83	10.99	10.99
NaO			.85	2.55	2.55
K_2O			.14	.89	.89
Cr_2O_3			.36	---	---
MnO			.25	.13	.13
TiO_2			.13	.97	.97
P_2O_5			.23	.28	.28
FeS			5.35	---	---
H_2O			.33	1.45	1.45

Table II.- Constricted-Arc Supersonic Jet Test Points

Test point	H_{AV}, j/kg	Impact pressure, newton/m^2	V_{eff}, m/sec	Effective altitude, m	$\frac{1}{2}\rho_{eff}V^3_{eff}$, W/m^2	$\dot{q}_{o\ calc}$, W/m^2	$\dot{q}_{o\ meas}$, W/m^2
A	127×10^6	240	19.4×10^3	98.5×10^3	2.33×10^6	2.2×10^6	1.50×10^6
B	50×10^6	400	13.0×10^3	91.5×10^3	2.60×10^6	2.5×10^6	1.71×10^6
C	67×10^6	507	14.0×10^3	91.0×10^3	3.53×10^6	3.0×10^6	2.24×10^6
D	83×10^6	550	14.8×10^3	91.2×10^3	4.07×10^6	3.2×10^6	2.62×10^6
E	44.6×10^6	10,000	13.4×10^3	72.5×10^3	67.00×10^6	31.5×10^6	32.1×10^6

Table III.- Test Schedule

Model no.	Material	Test point	Initial mass, grams	Final mass, grams	Exposure time, sec	Remarks
49	Steel	B	63.78	62.44	45	
50	Steel	B	64.35	13.52	120	
51	Steel	D	63.88	6.22	57	
52	Steel	A	63.529	63.545	55	Gained 0.016 grams
53	Steel	A	63.75	57.95	90	
54	Basalt	D	22.08	22.47	45	Gained 0.39 grams
55	Gabbro	D	22.73	17.55	45	
56	Steel	D	63.89	13.20	50	
57	Steel	D	63.53	13.20	40	
58	Iron Met.	B	62.22	58.20	45	
59	Iron Met.	C	47.56	32.17	45	
60	Iron Met.	D	63.56	47.74	32.5	
61	Iron Met.	A	61.72	56.48	120	
62	Stone Met.	B	22.75	21.05	45	
64	Steel	C	63.58	35.88	50	
66	Steel	B	63.95	61.99	49	
67	Steel	D	64.04	43.25	39	
68	Stone Met.	D	21.89	5.60	60	
70	Stone Met.	C	23.52	9.35	55	
72	Stone Met.	A	20.57	18.95	45	
73	Iron Met.	A	63.48	49.15	120	
74	Gabbro	A	22.49	20.00	62	
75	Gabbro	D	22.33	21.08	47.5	
76	Gabbro	C	23.66	22.50	49	
78	Basalt	B	22.35	21.93	53	
79	Basalt	D	21.67	21.09	46	
80	Basalt	A	17.89	15.94	60	
81	Gabbro	B	22.08	21.37	61	
82	Stone Met.	E	28.97	20.25	11	
83	Steel	E	64.00	37.1	7.2	
84	Gabbro	E	22.94	10.30	7	
85	Basalt	E	22.75	19.36	3	Fractured at 3.0 sec

Table IV.- Typical Artificial Meteor Foam Density

Material	Test condition	Initial density, kg/m^3	Foam density, kg/m^3	$\frac{\text{Foam density}}{\text{Initial density}}$
Steel	D	7,870	4,730	0.61
Iron Met.	C	7,800	4,370	0.56
Stone Met.	A	3,590	1,725	0.48
Stone Met.	C	3,590	1,390	0.39
Stone Met.	E	3,590	1,290	0.36
Gabbro	C	2,920	1,076	0.37
Gabbro	E	2,920	800	0.27

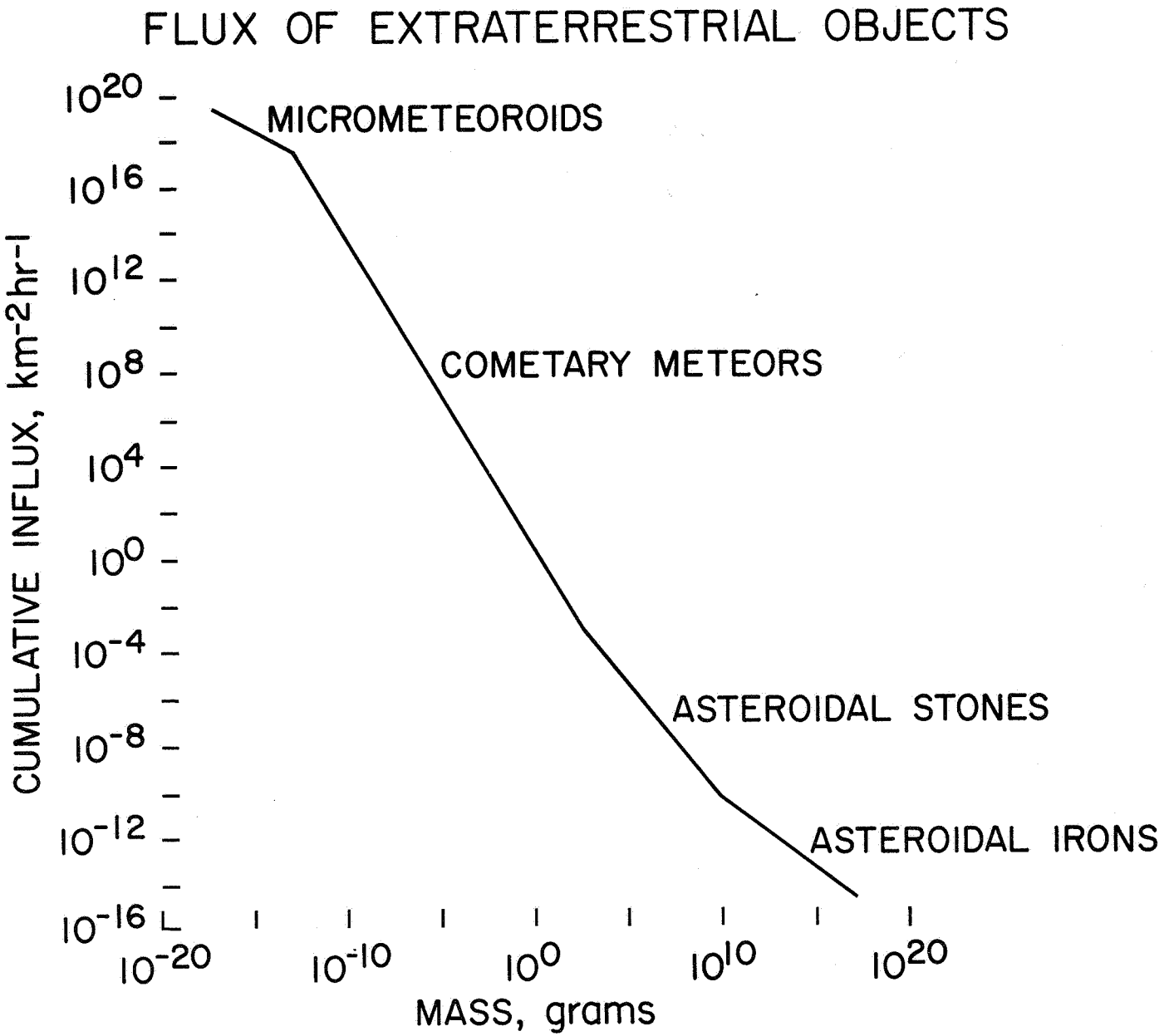

Fig. 1

NATIONAL AERONAUTICS AND SPACE ADMINISTRATION
AMES RESEARCH CENTER, MOFFETT FIELD, CALIFORNIA

TYPICAL METEOR TRAJECTORIES

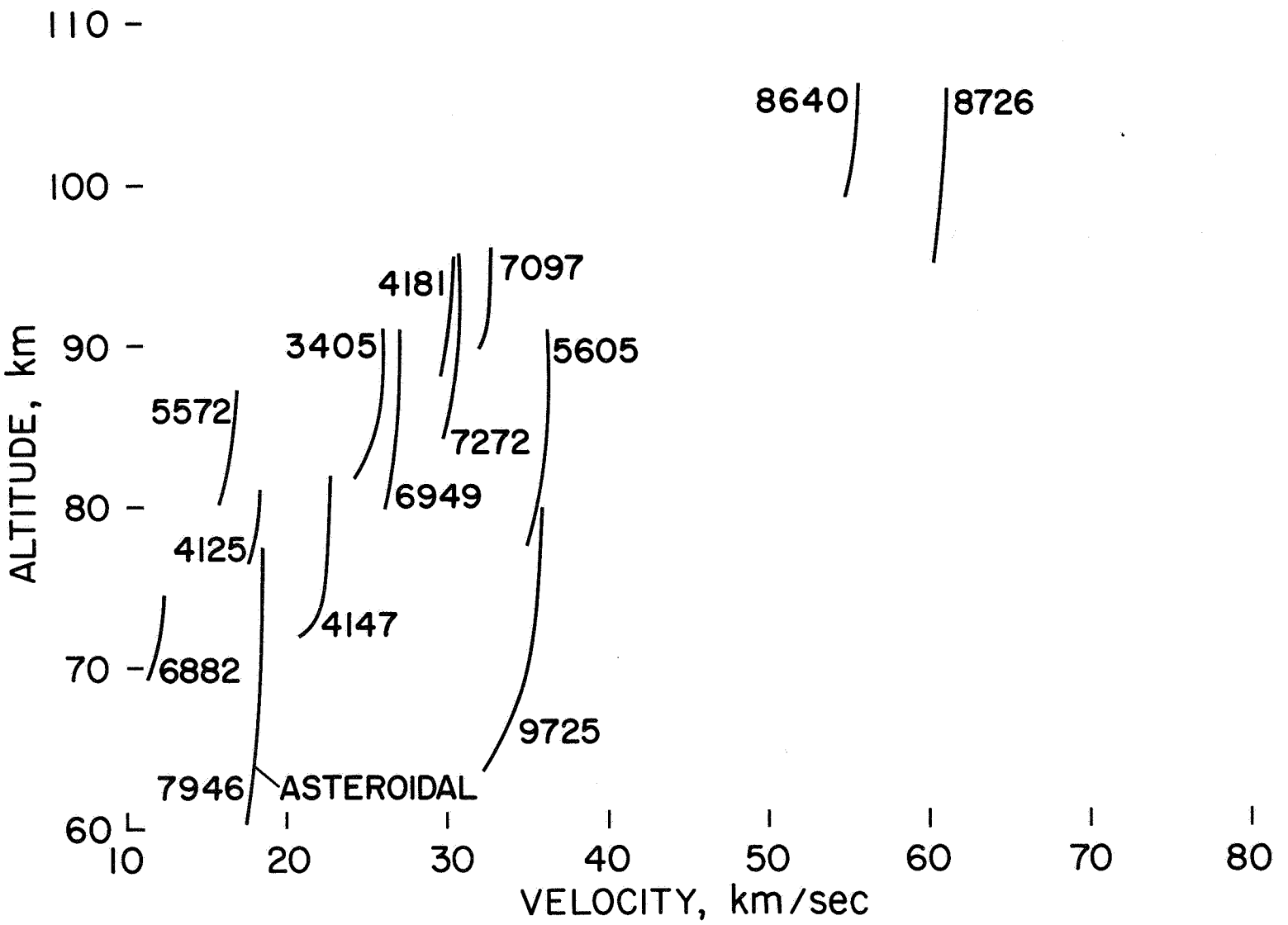

Fig. 2

NATIONAL AERONAUTICS AND SPACE ADMINISTRATION
AMES RESEARCH CENTER, MOFFETT FIELD, CALIFORNIA

TYPICAL VALUES OF BALLISTIC PARAMETER AS A FUNCTION OF ALTITUDE

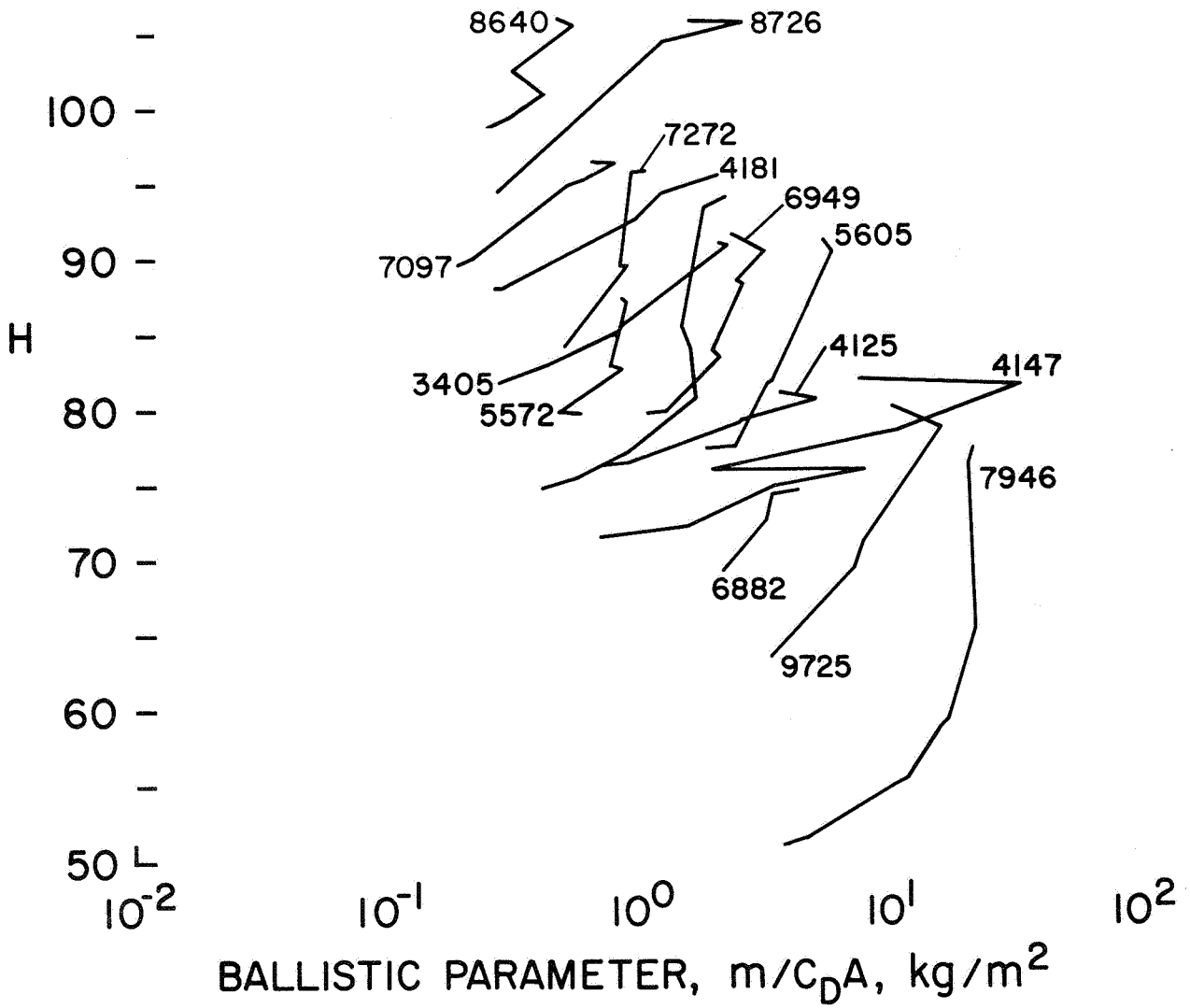

Fig. 3

NATIONAL AERONAUTICS AND SPACE ADMINISTRATION
AMES RESEARCH CENTER, MOFFETT FIELD, CALIFORNIA

SCHEMATIC DRAWING OF A CONSTRICTED-ARC SUPERSONIC JET

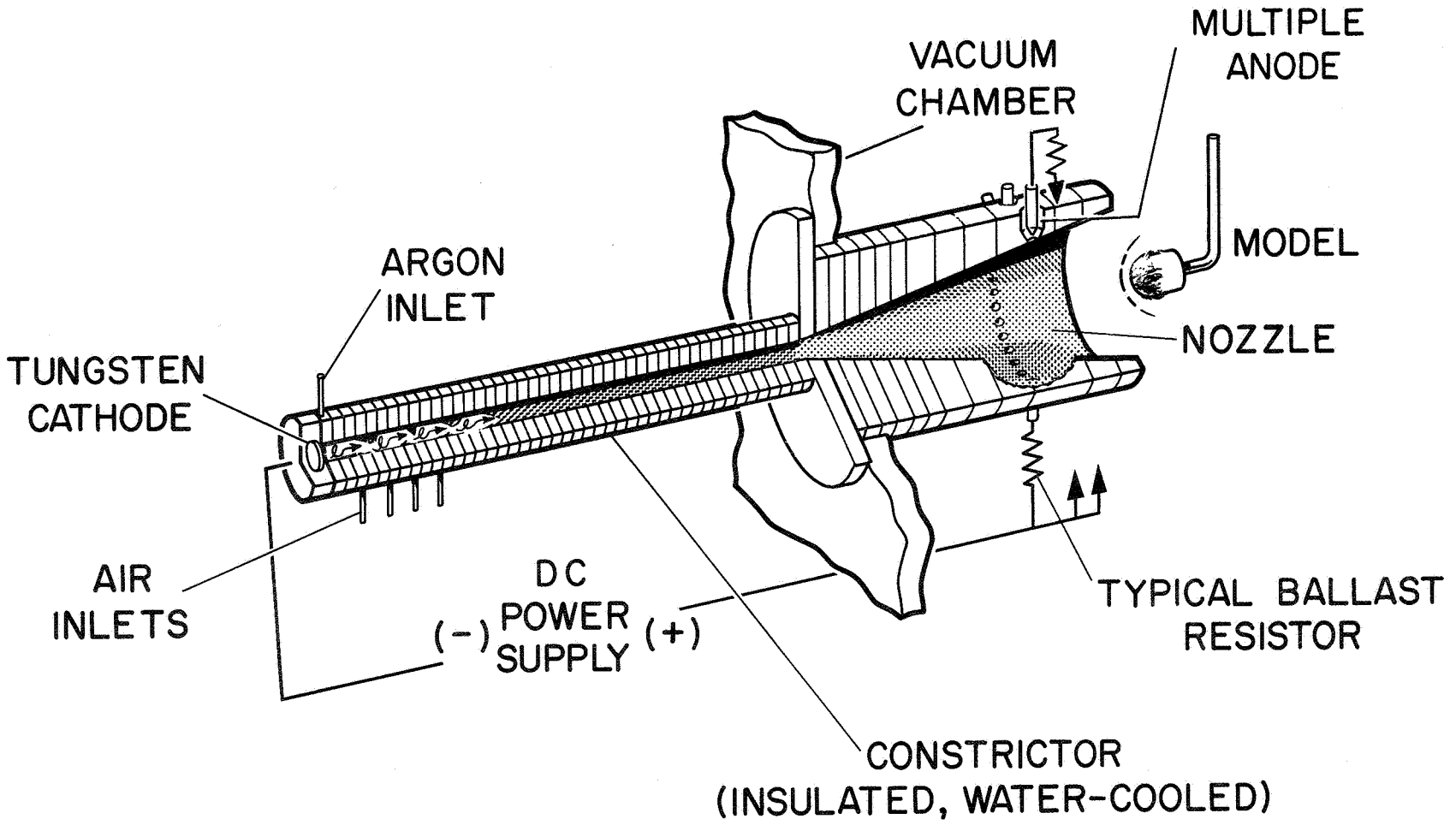

Fig. 4

NATIONAL AERONAUTICS AND SPACE ADMINISTRATION
AMES RESEARCH CENTER, MOFFETT FIELD, CALIFORNIA

CONSTRICTED-ARC SUPERSONIC-JET APPARATUS
2.54 cm dia ARC-HEATED PLANETARY GAS WIND TUNNEL

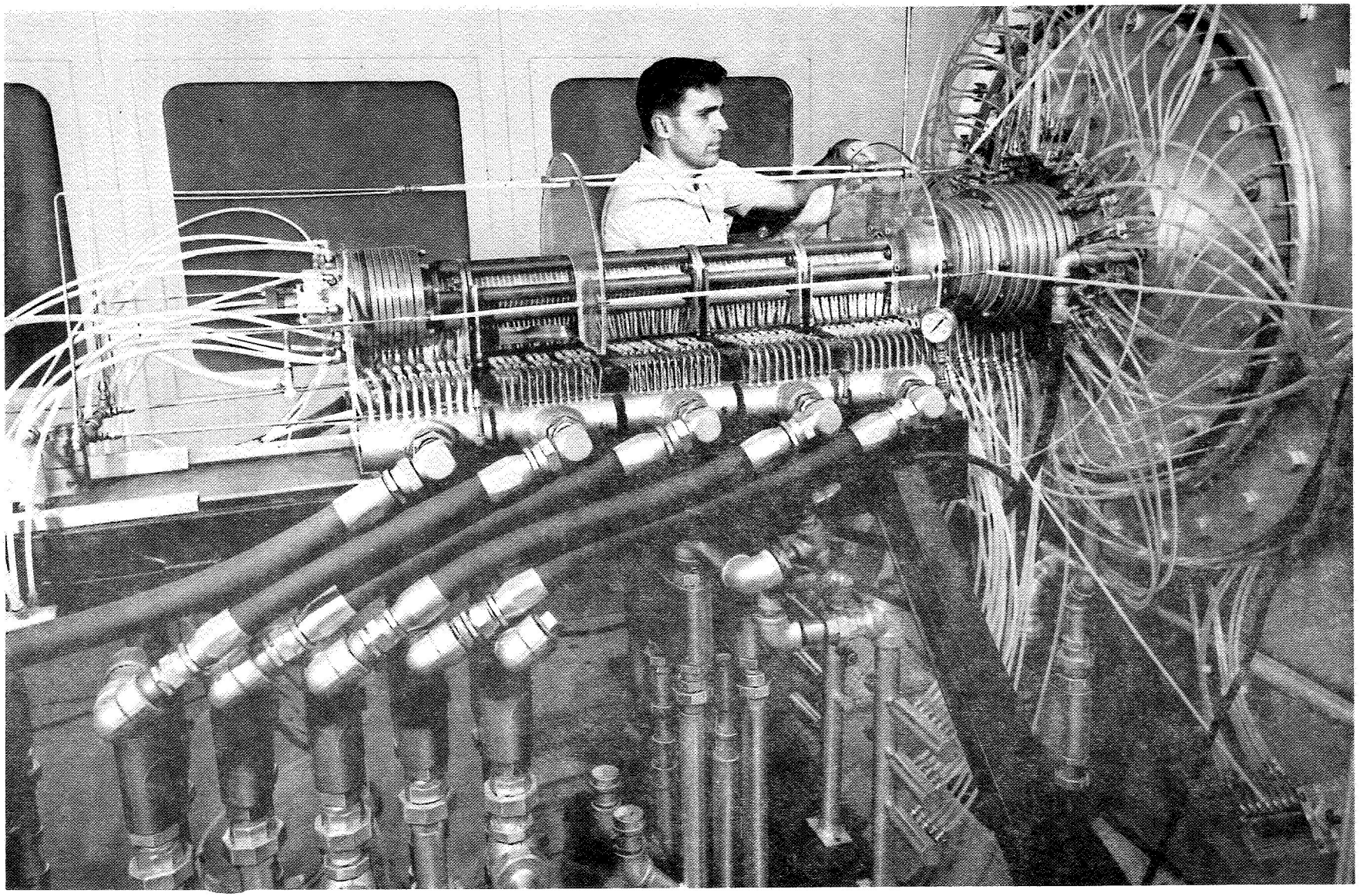

Fig. 5(a)

A-33748.1

NATIONAL AERONAUTICS AND SPACE ADMINISTRATION
AMES RESEARCH CENTER, MOFFETT FIELD, CALIFORNIA

CONSTRICTED-ARC SUPERSONIC-JET APPARATUS

1.27 cm dia. CONSTRICTED-ARC SUPERSONIC JET

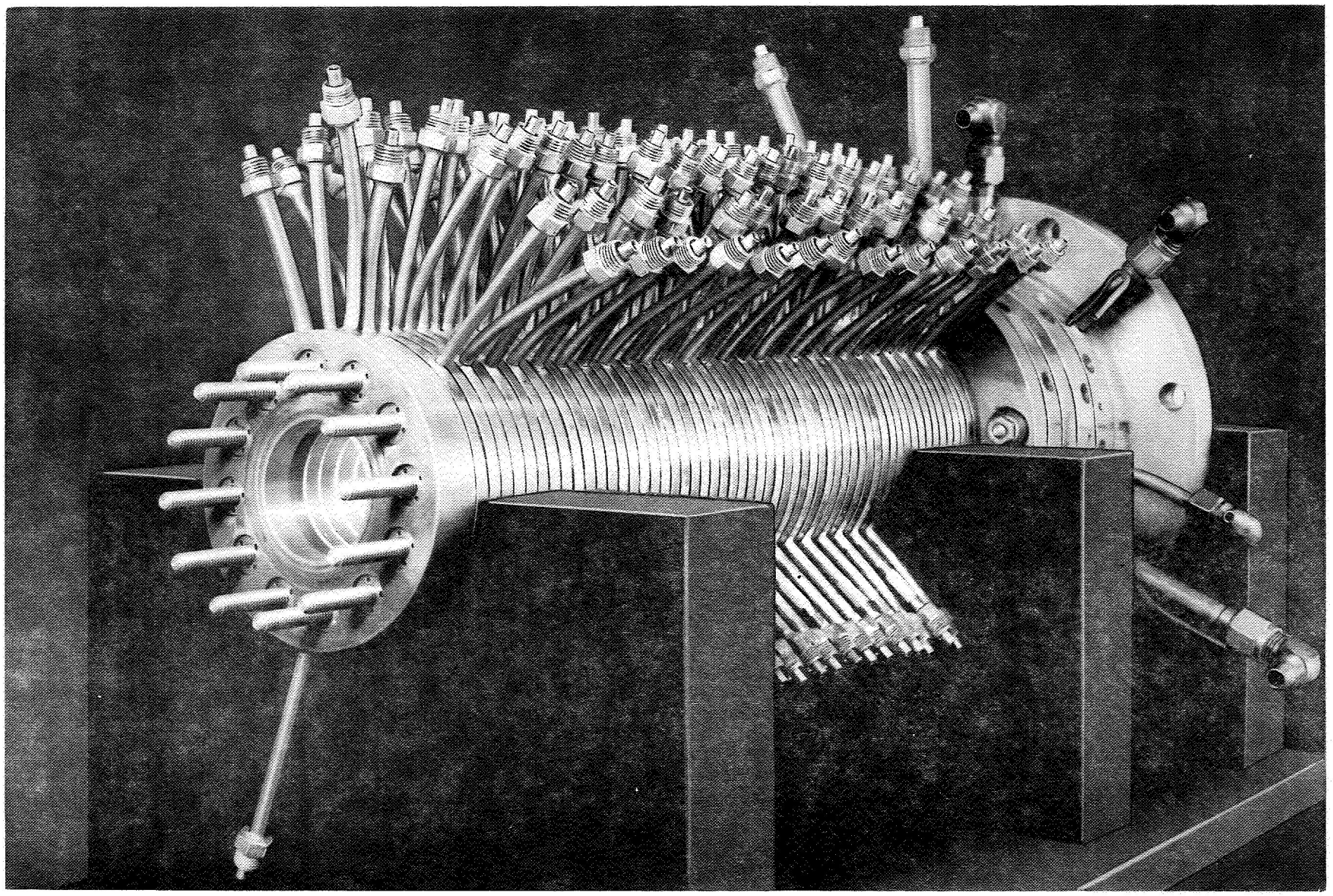

Fig. 5(b)

A-36962.1

NATIONAL AERONAUTICS AND SPACE ADMINISTRATION
AMES RESEARCH CENTER, MOFFETT FIELD, CALIFORNIA

CONSTRICTED-ARC SUPERSONIC-JET ENTHALPY AS A FUNCTION OF IMPACT PRESSURE

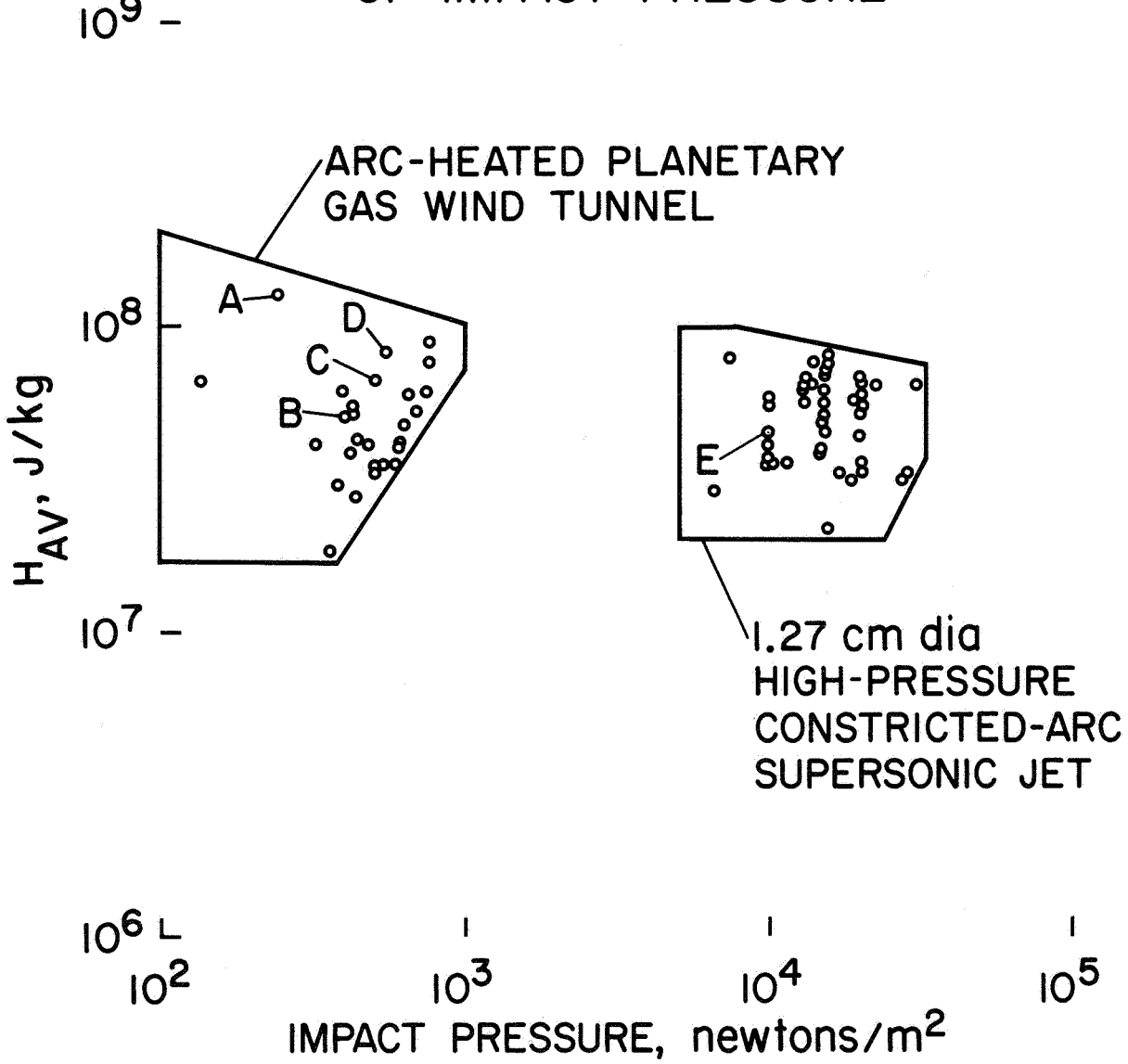

Fig. 6

NATIONAL AERONAUTICS AND SPACE ADMINISTRATION
AMES RESEARCH CENTER, MOFFETT FIELD, CALIFORNIA

TYPICAL RADIAL FLOW PROFILES OF CONSTRICTED-ARC SUPERSONIC-JET
CONDITION B

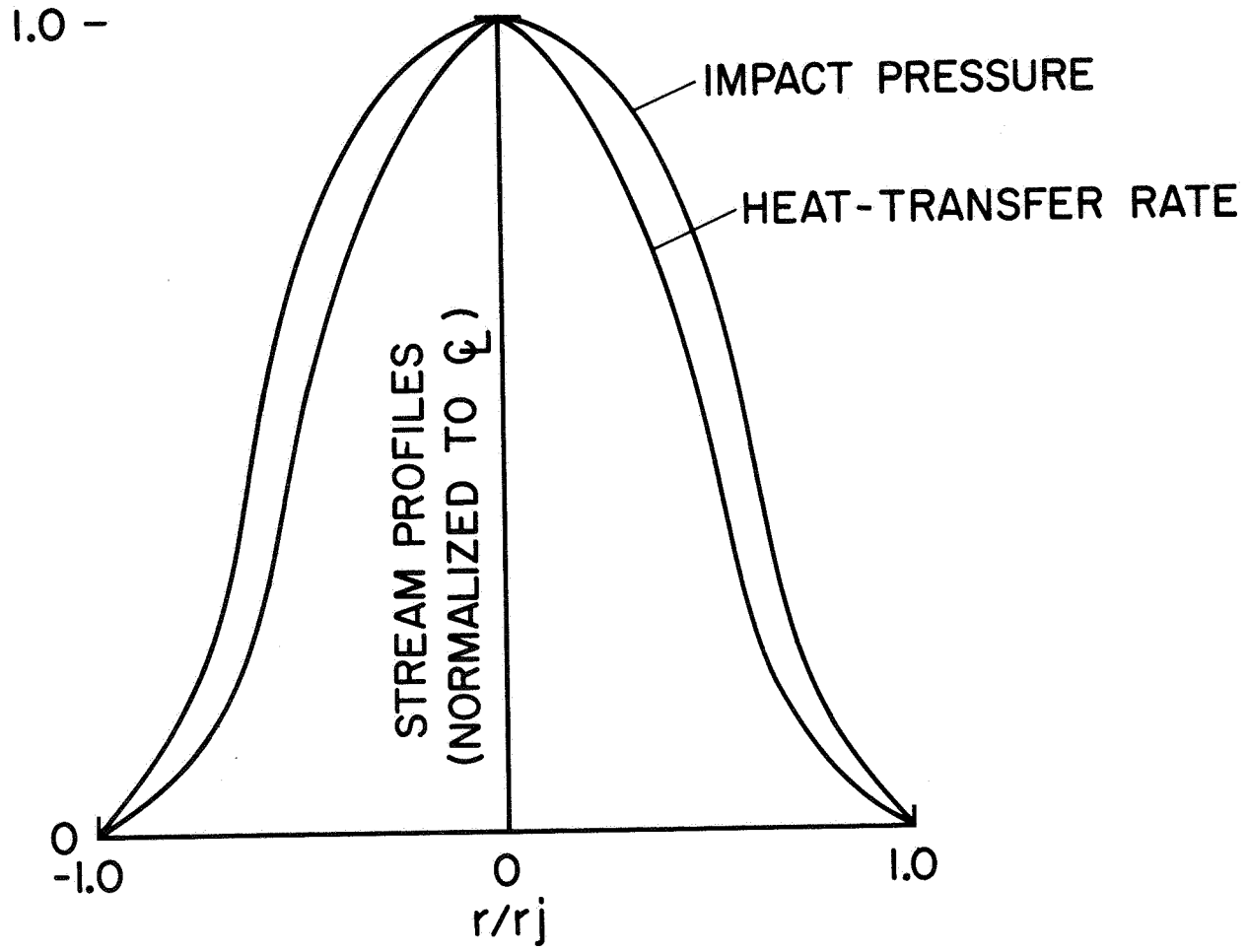

Fig. 7

NATIONAL AERONAUTICS AND SPACE ADMINISTRATION
AMES RESEARCH CENTER, MOFFETT FIELD, CALIFORNIA

COVERAGE OF METEOR FLIGHT REGIME ACHIEVED BY CONSTRICTED-ARC APPARATUS

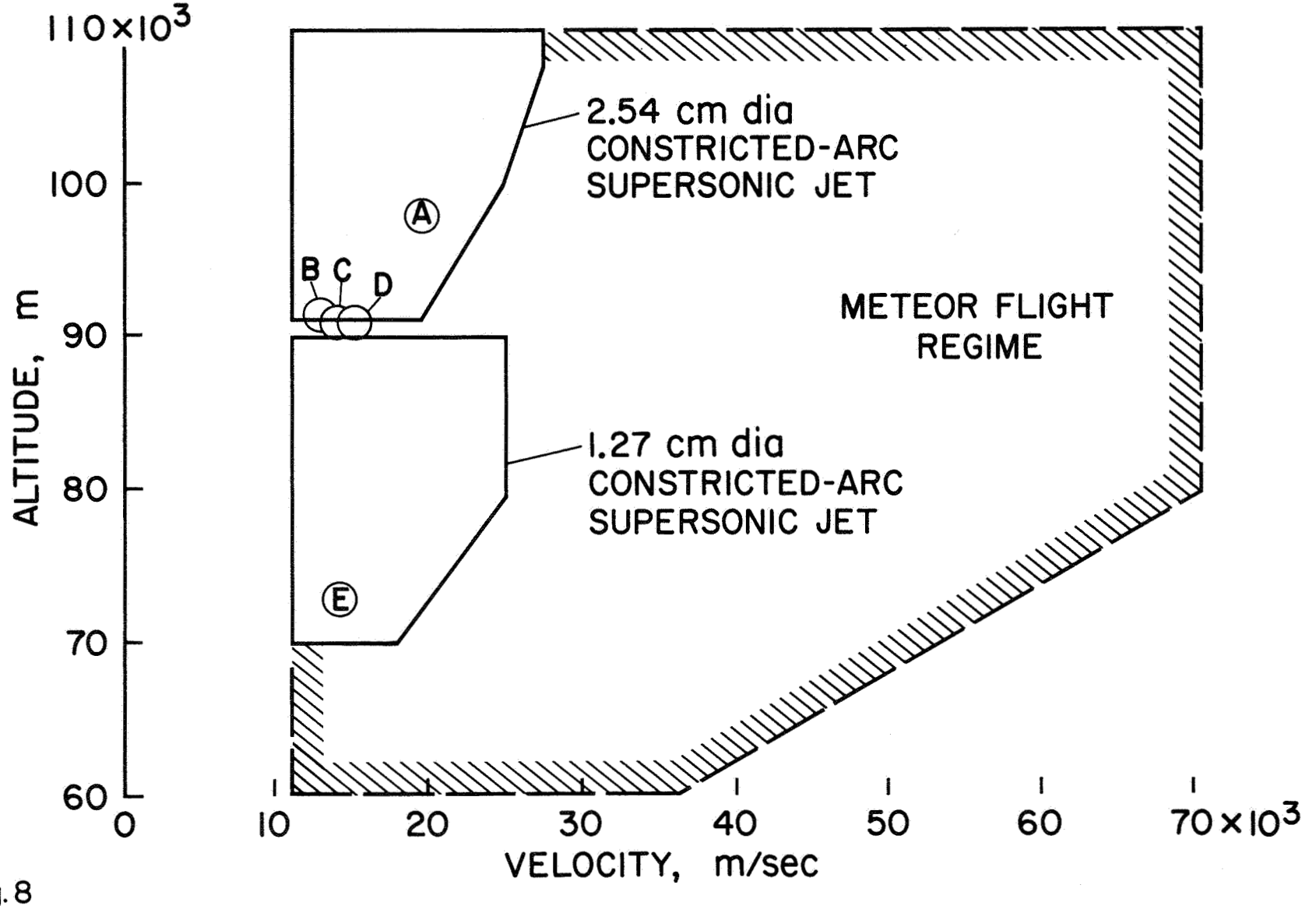

Fig. 8

NATIONAL AERONAUTICS AND SPACE ADMINISTRATION
AMES RESEARCH CENTER, MOFFETT FIELD, CALIFORNIA

STANDARD TEST MODEL DIMENSIONS

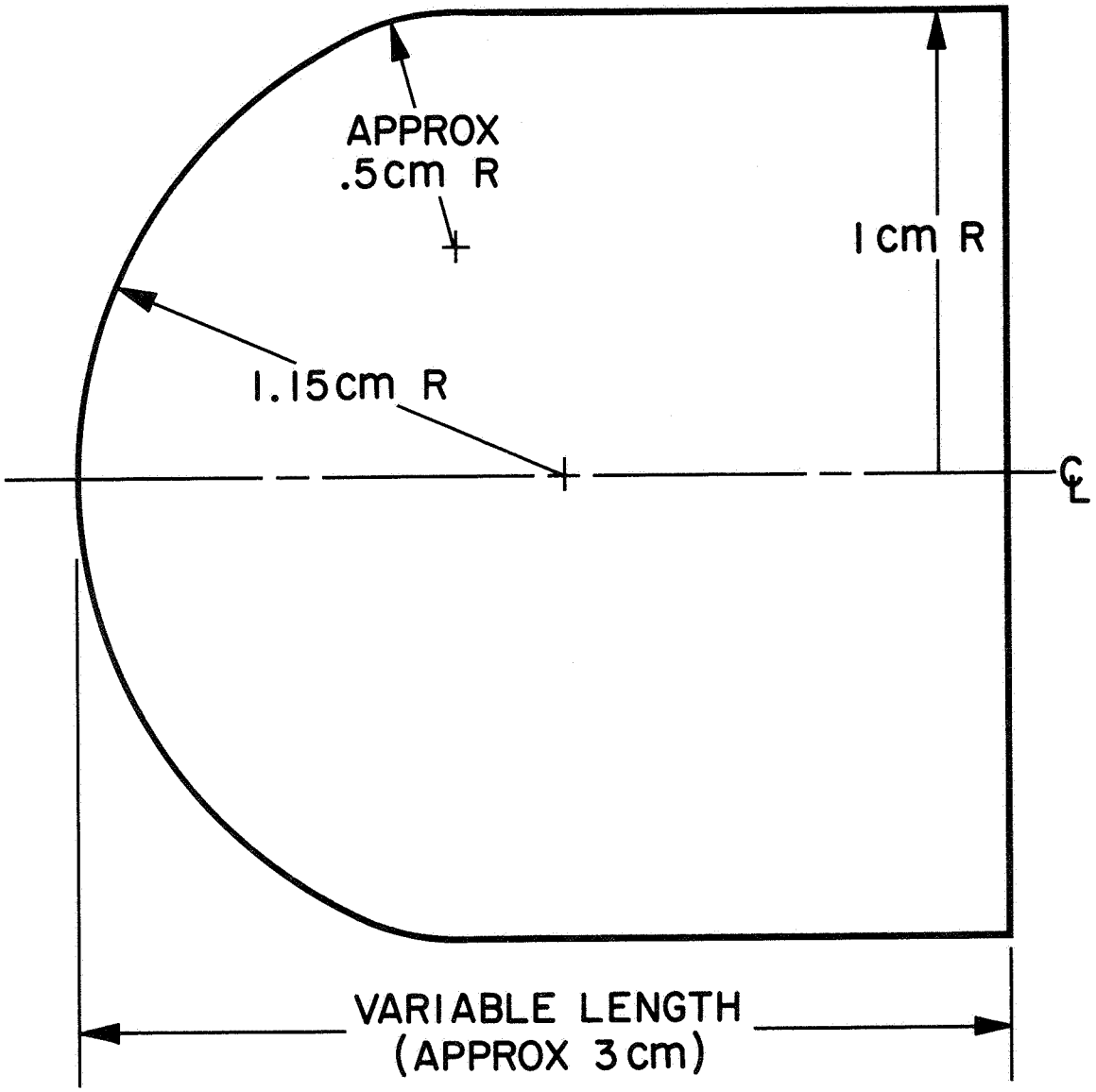

Fig. 9

NATIONAL AERONAUTICS AND SPACE ADMINISTRATION
AMES RESEARCH CENTER, MOFFETT FIELD, CALIFORNIA

RADIATION INSTRUMENTATION FOR ARC-HEATED PLANETARY GAS WIND TUNNEL

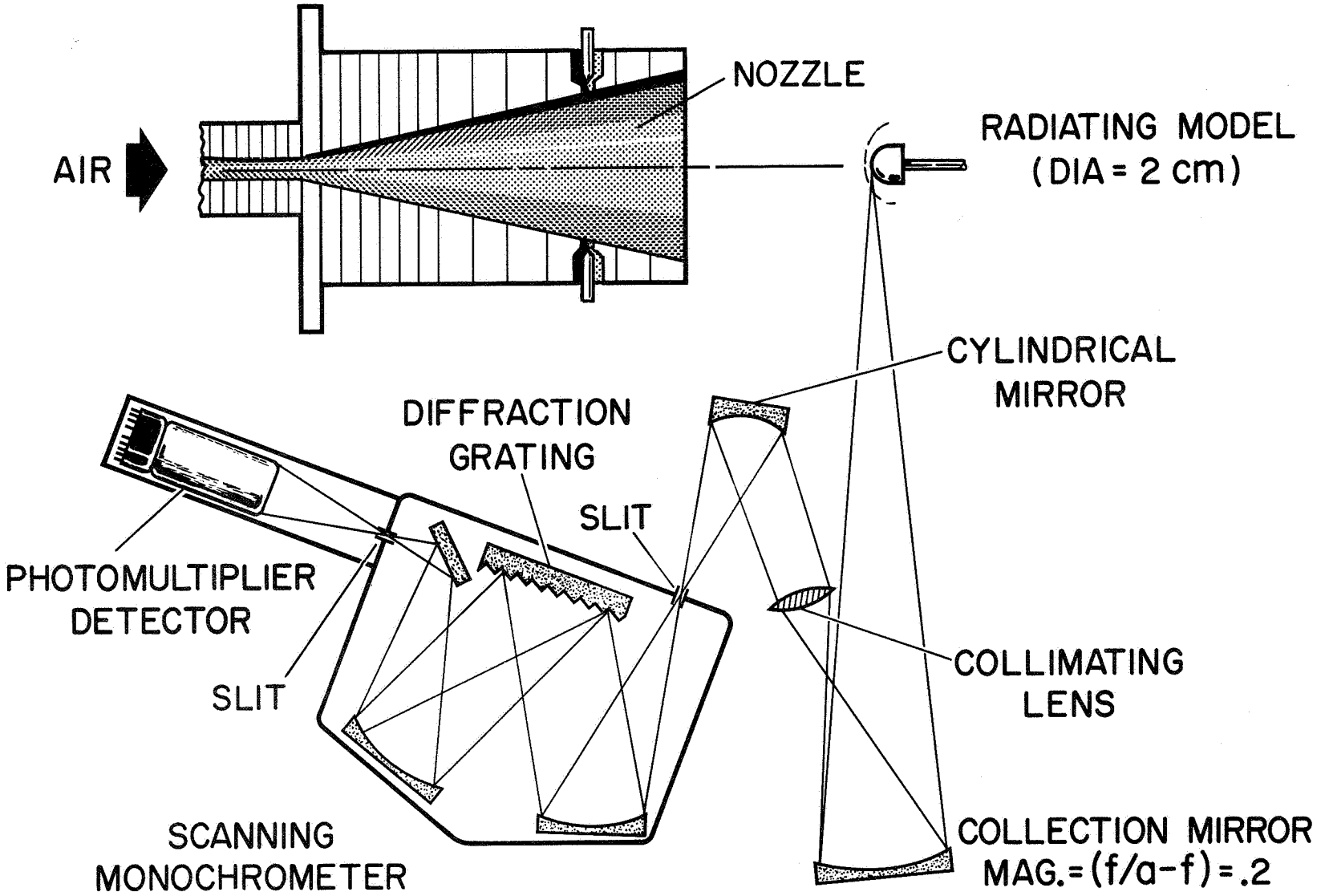

Fig. 10

NATIONAL AERONAUTICS AND SPACE ADMINISTRATION
AMES RESEARCH CENTER, MOFFETT FIELD, CALIFORNIA

FLANGE FORMATION ON IRON METEORITE, STEEL AND STONE METEORITE MODELS

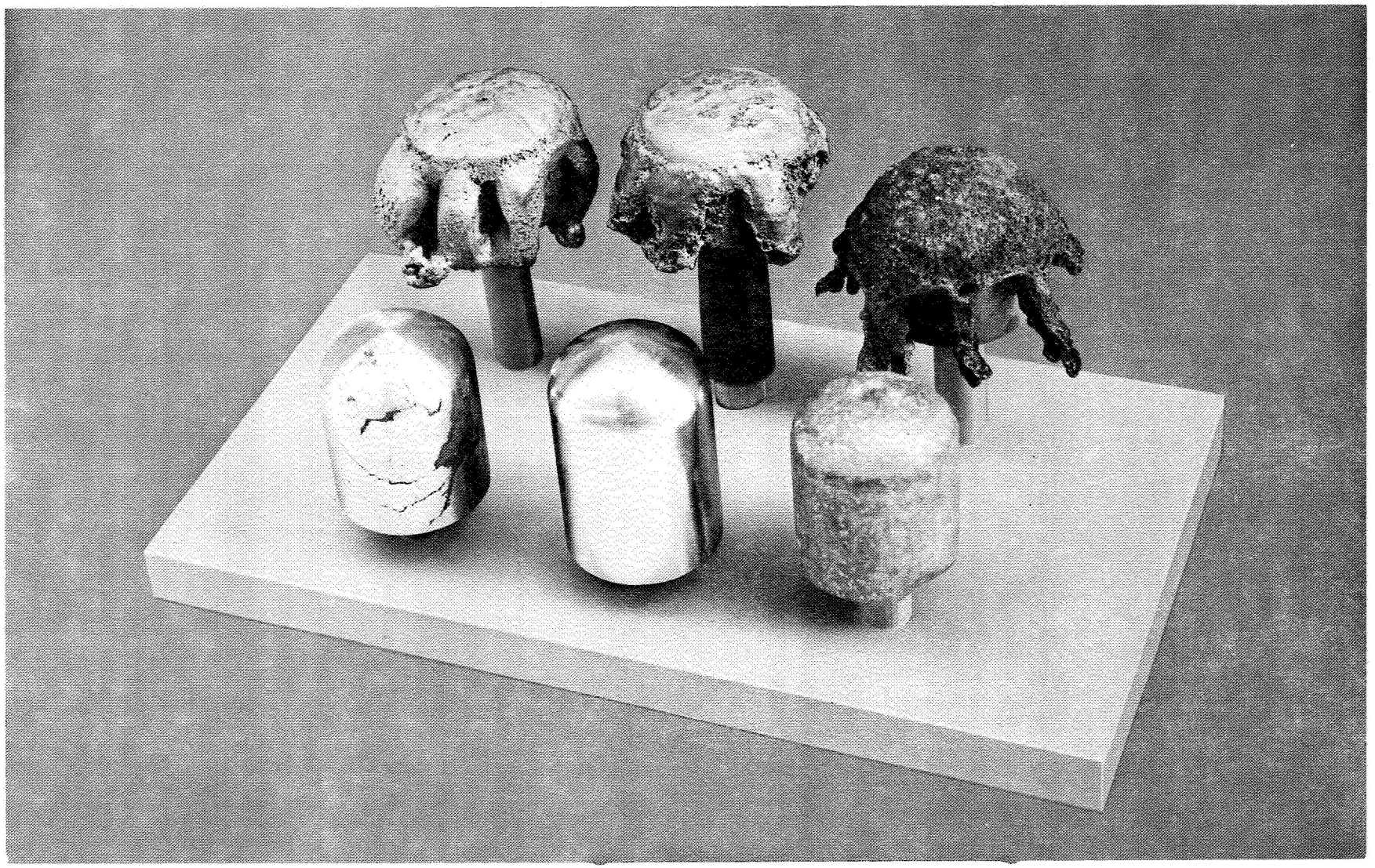

Fig. 11

A-36961.1

NATIONAL AERONAUTICS AND SPACE ADMINISTRATION
AMES RESEARCH CENTER, MOFFETT FIELD, CALIFORNIA

VARIATION OF FRONTAL AREA WITH TIME FOR VARIOUS SIMULATED ALTITUDES AND VELOCITIES

STEEL MODELS

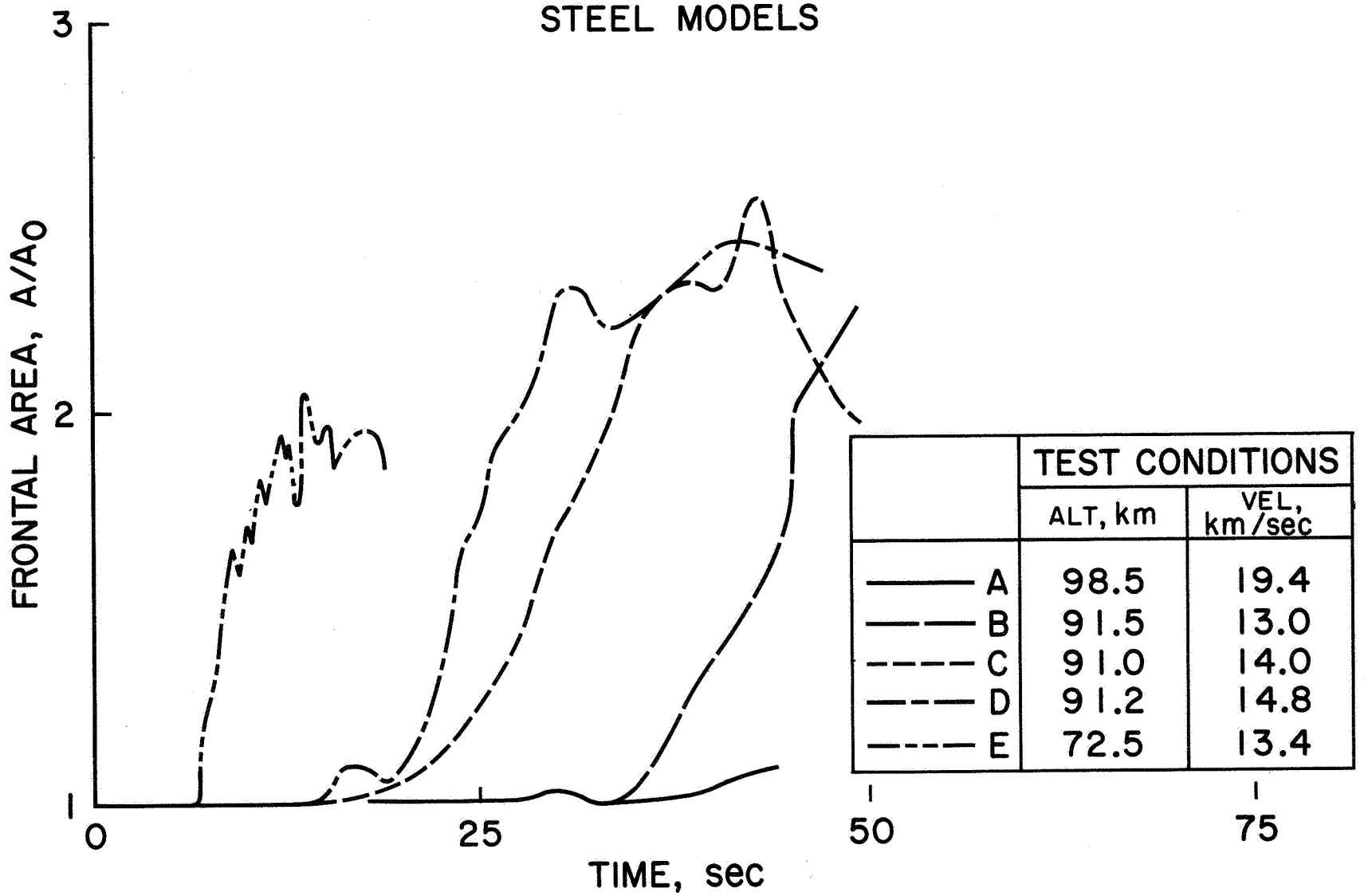

Fig. 12(a)

NATIONAL AERONAUTICS AND SPACE ADMINISTRATION
AMES RESEARCH CENTER, MOFFETT FIELD, CALIFORNIA

VARIATION OF FRONTAL AREA WITH TIME FOR VARIOUS SIMULATED ALTITUDES AND VELOCITIES

STONE METEORITE MODELS

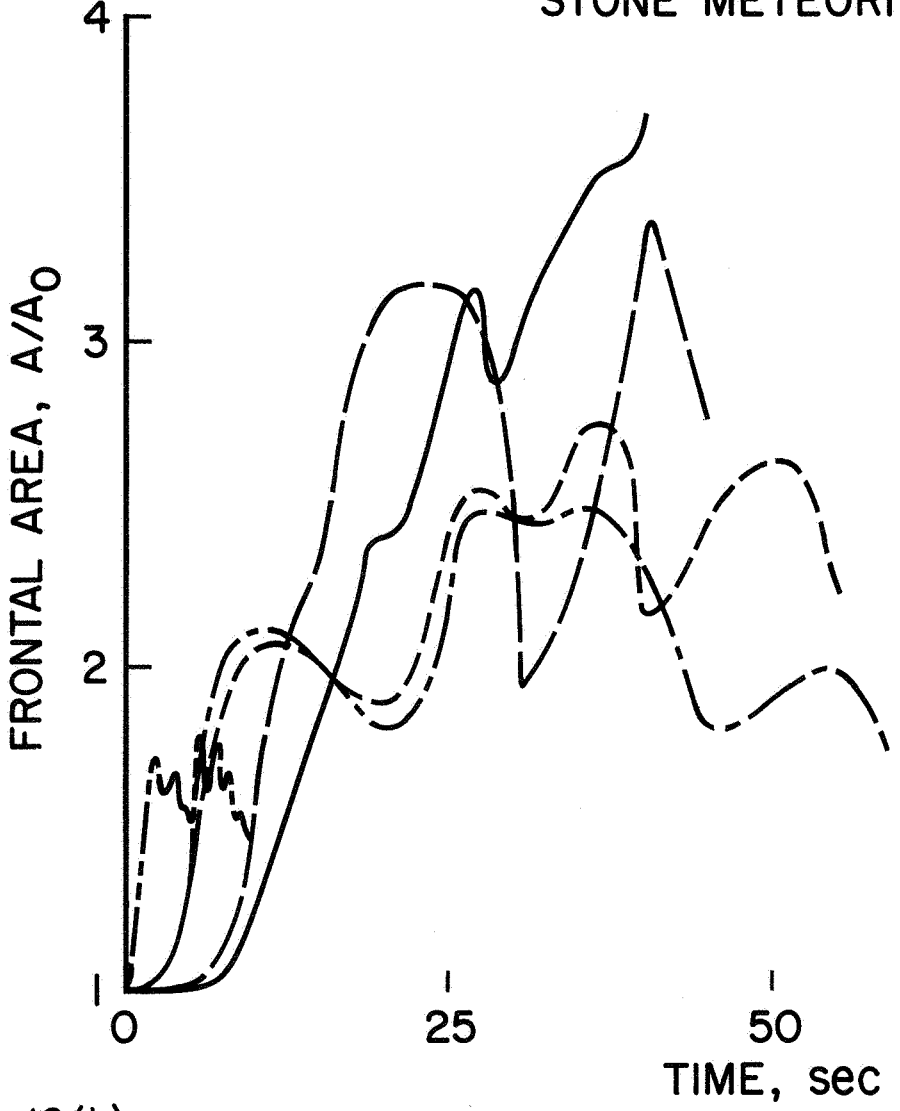

	TEST CONDITIONS	
	ALT, km	VEL, km/sec
A	98.5	19.6
B	91.5	13.0
C	91.0	14.0
D	91.2	14.8
E	72.5	13.4

Fig. 12 (b)

NATIONAL AERONAUTICS AND SPACE ADMINISTRATION
AMES RESEARCH CENTER, MOFFETT FIELD, CALIFORNIA

VARIATION OF FRONTAL AREA WITH TIME FOR VARIOUS SIMULATED ALTITUDES AND VELOCITIES

COMPARISON OF STEEL AND IRON METEORITE MODELS

TEST CONDITION D

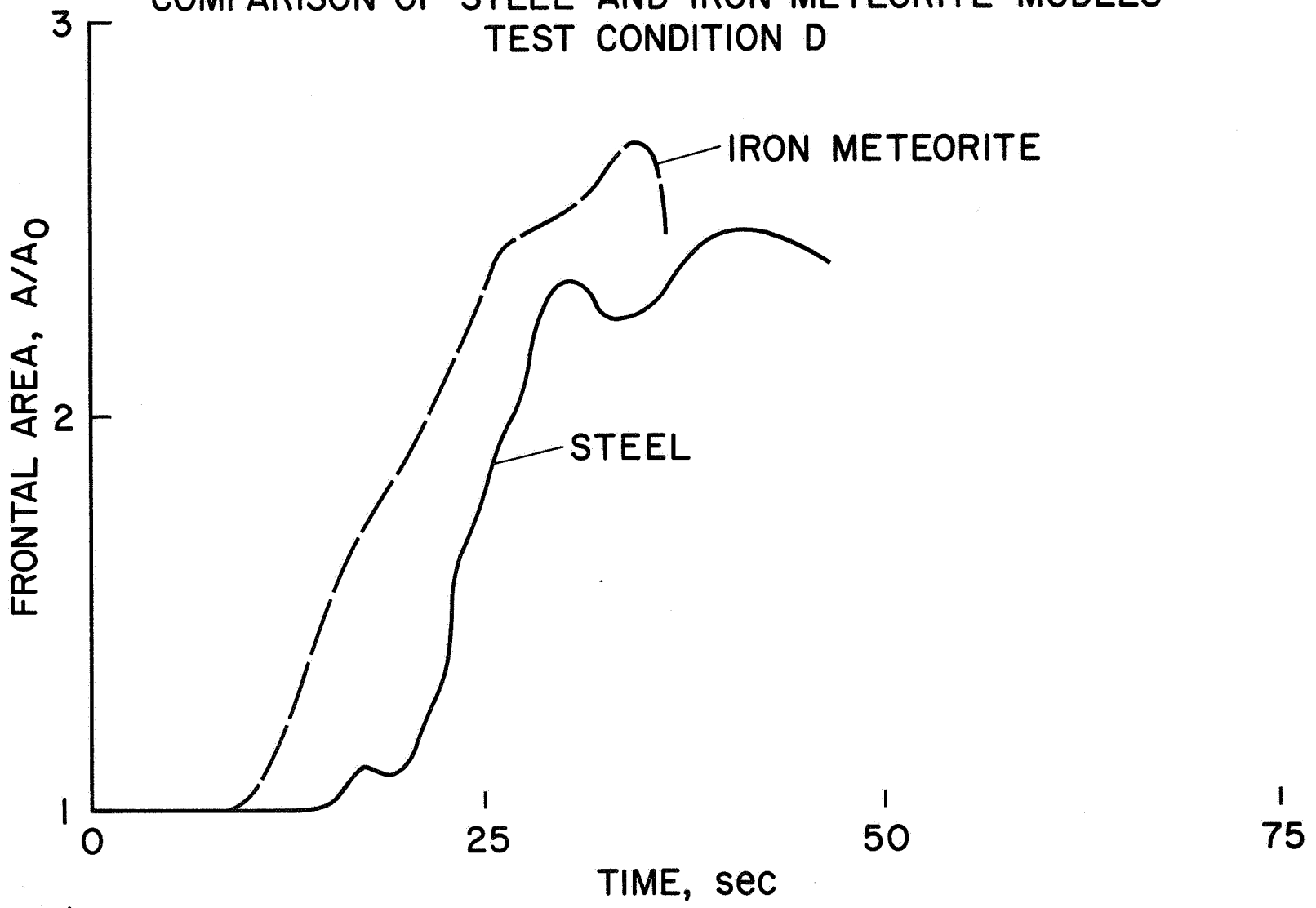

Fig. 12(c)

NATIONAL AERONAUTICS AND SPACE ADMINISTRATION
AMES RESEARCH CENTER, MOFFETT FIELD, CALIFORNIA

VARIATION OF FRONTAL AREA WITH TIME FOR VARIOUS SIMULATED ALTITUDES AND VELOCITIES

COMPARISON OF EARTH STONE (GABBRO AND BASALT) AND STONE METEORITE

TEST CONDITION D

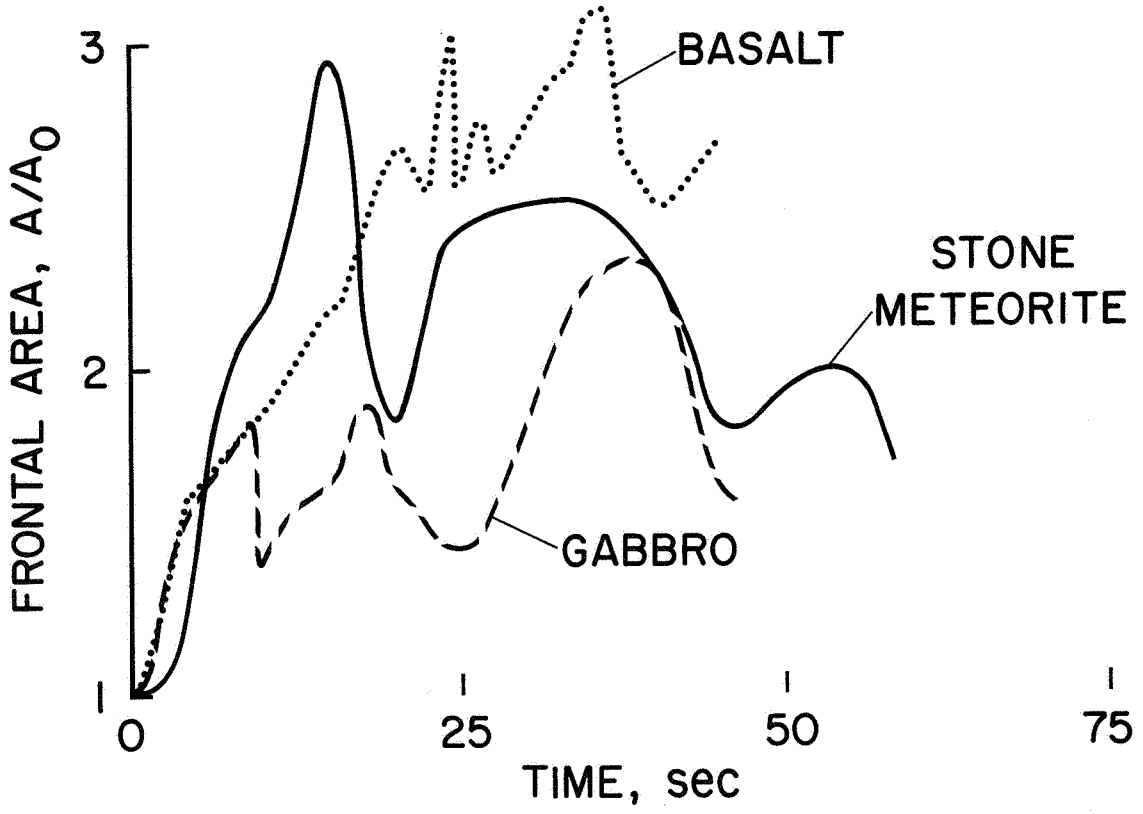

Fig. 12 (d)

NATIONAL AERONAUTICS AND SPACE ADMINISTRATION
AMES RESEARCH CENTER, MOFFETT FIELD, CALIFORNIA

VARIATION OF MODEL LENGTH WITH TIME FOR VARIOUS SIMULATED ALTITUDES AND VELOCITIES

STEEL MODELS

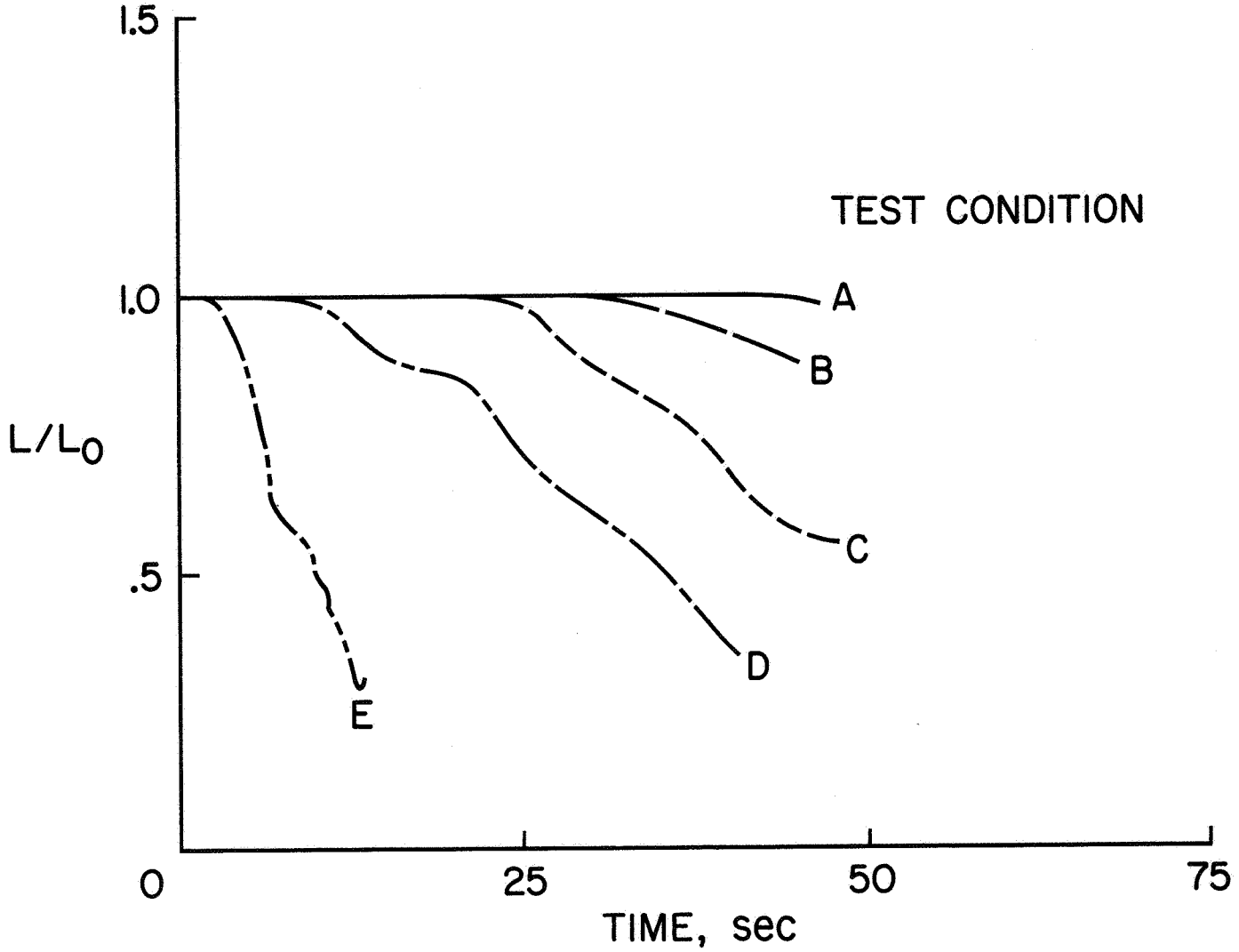

Fig. 13(a)

NATIONAL AERONAUTICS AND SPACE ADMINISTRATION
AMES RESEARCH CENTER, MOFFETT FIELD, CALIFORNIA

VARIATION OF MODEL LENGTH WITH TIME FOR VARIOUS SIMULATED ALTITUDES AND VELOCITIES

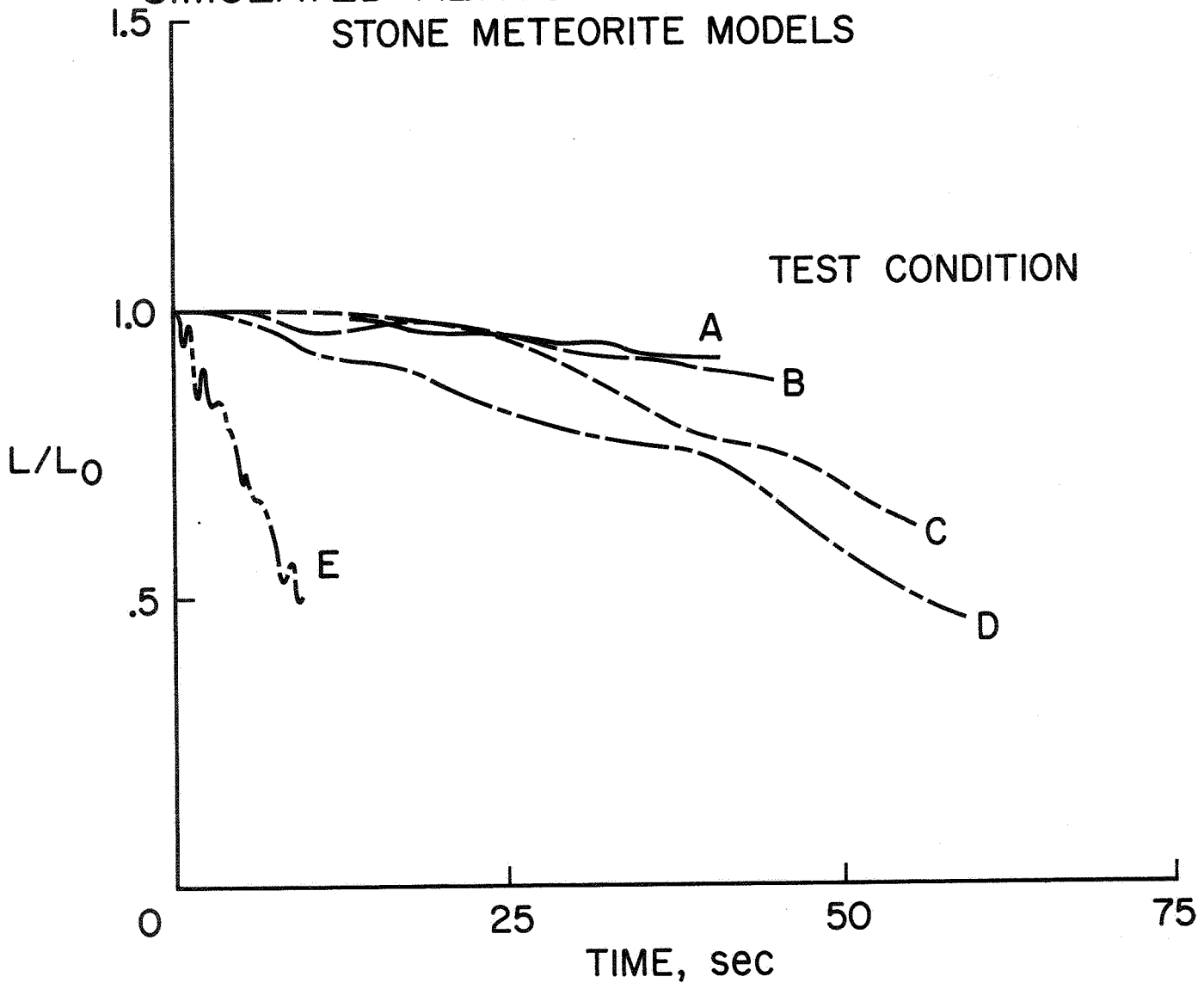

Fig. 13(b)

NATIONAL AERONAUTICS AND SPACE ADMINISTRATION
AMES RESEARCH CENTER, MOFFETT FIELD, CALIFORNIA

VARIATION OF MODEL LENGTH WITH TIME FOR VARIOUS SIMULATED ALTITUDES AND VELOCITIES
COMPARISON OF STEEL AND IRON METEORITE MODELS
TEST CONDITION D

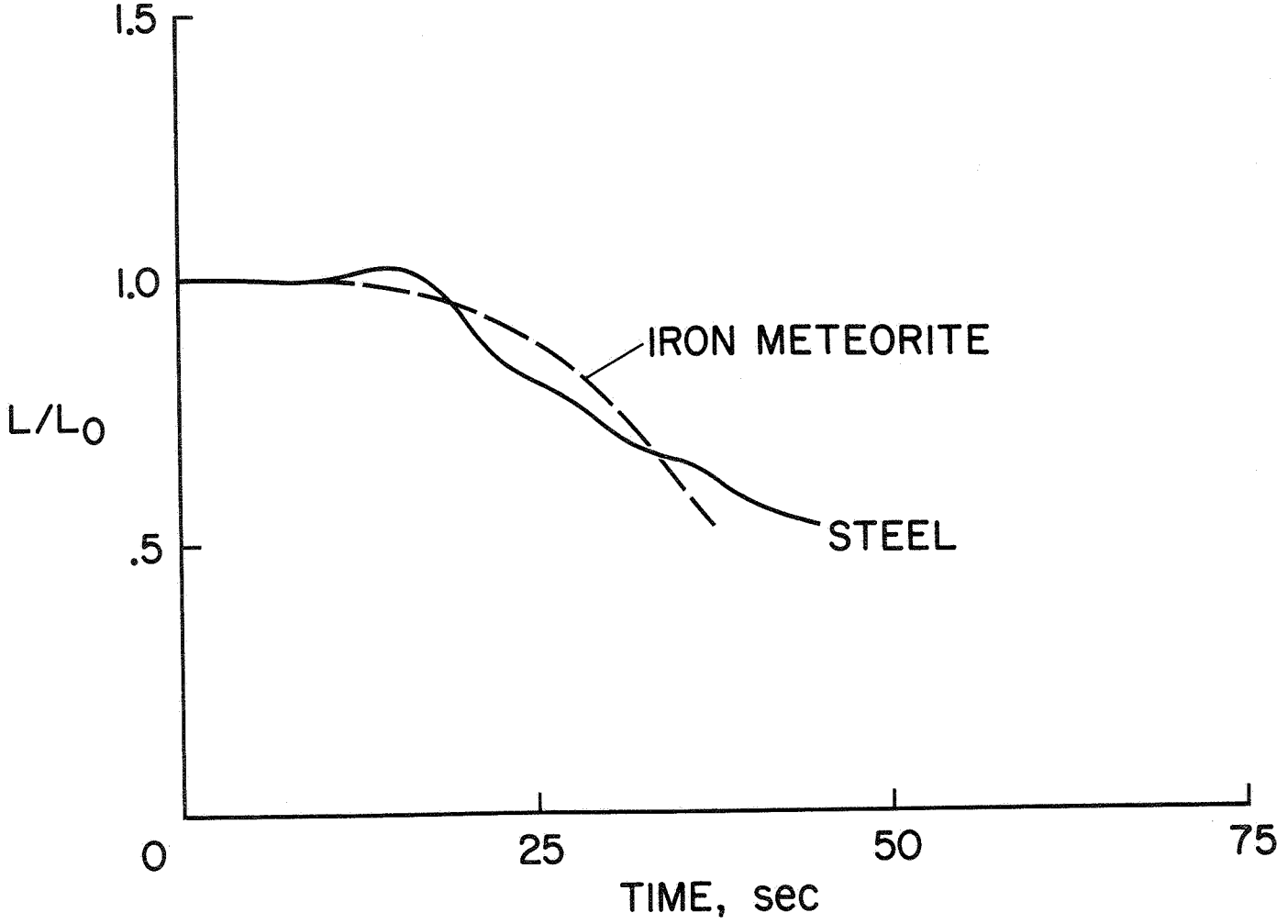

Fig. 13(c)

NATIONAL AERONAUTICS AND SPACE ADMINISTRATION
AMES RESEARCH CENTER, MOFFETT FIELD, CALIFORNIA

VARIATION OF MODEL LENGTH WITH TIME FOR VARIOUS SIMULATED ALTITUDES AND VELOCITIES

COMPARISON OF EARTH STONE (GABBRO AND BASALT) AND STONE METEORITE MODELS

TEST CONDITION D

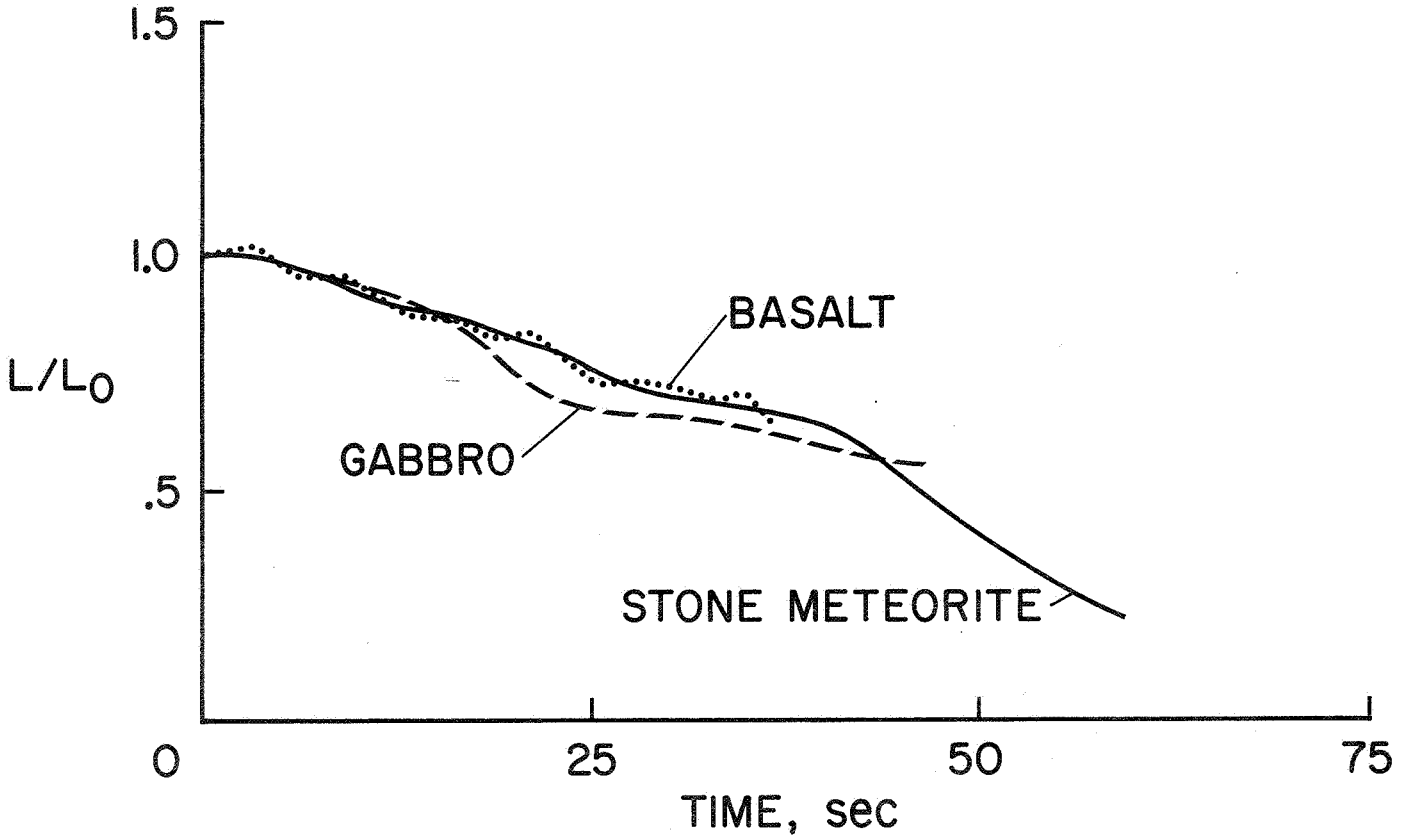

Fig. 13(d)

NATIONAL AERONAUTICS AND SPACE ADMINISTRATION
AMES RESEARCH CENTER, MOFFETT FIELD, CALIFORNIA

EFFECTIVE HEAT OF ABLATION AS A FUNCTION OF FOURIER MODULUS

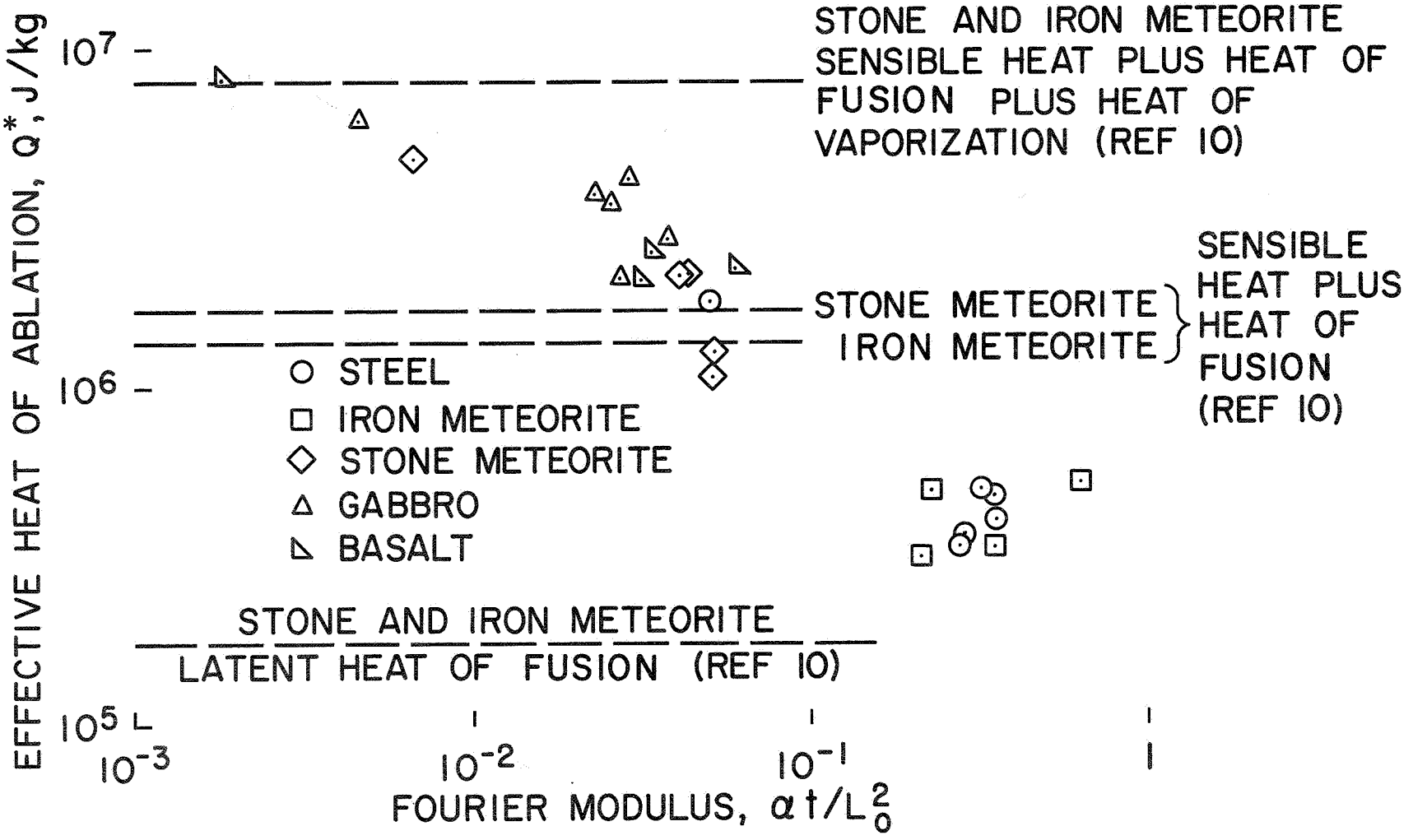

Fig. 14

NATIONAL AERONAUTICS AND SPACE ADMINISTRATION
AMES RESEARCH CENTER, MOFFETT FIELD, CALIFORNIA

LUMINOUS INTENSITY NORMALIZED TO 100 km DISTANCE

COMPARISON OF GABBRO, BASALT AND STONE METEORITE MODELS

TEST CONDITION D

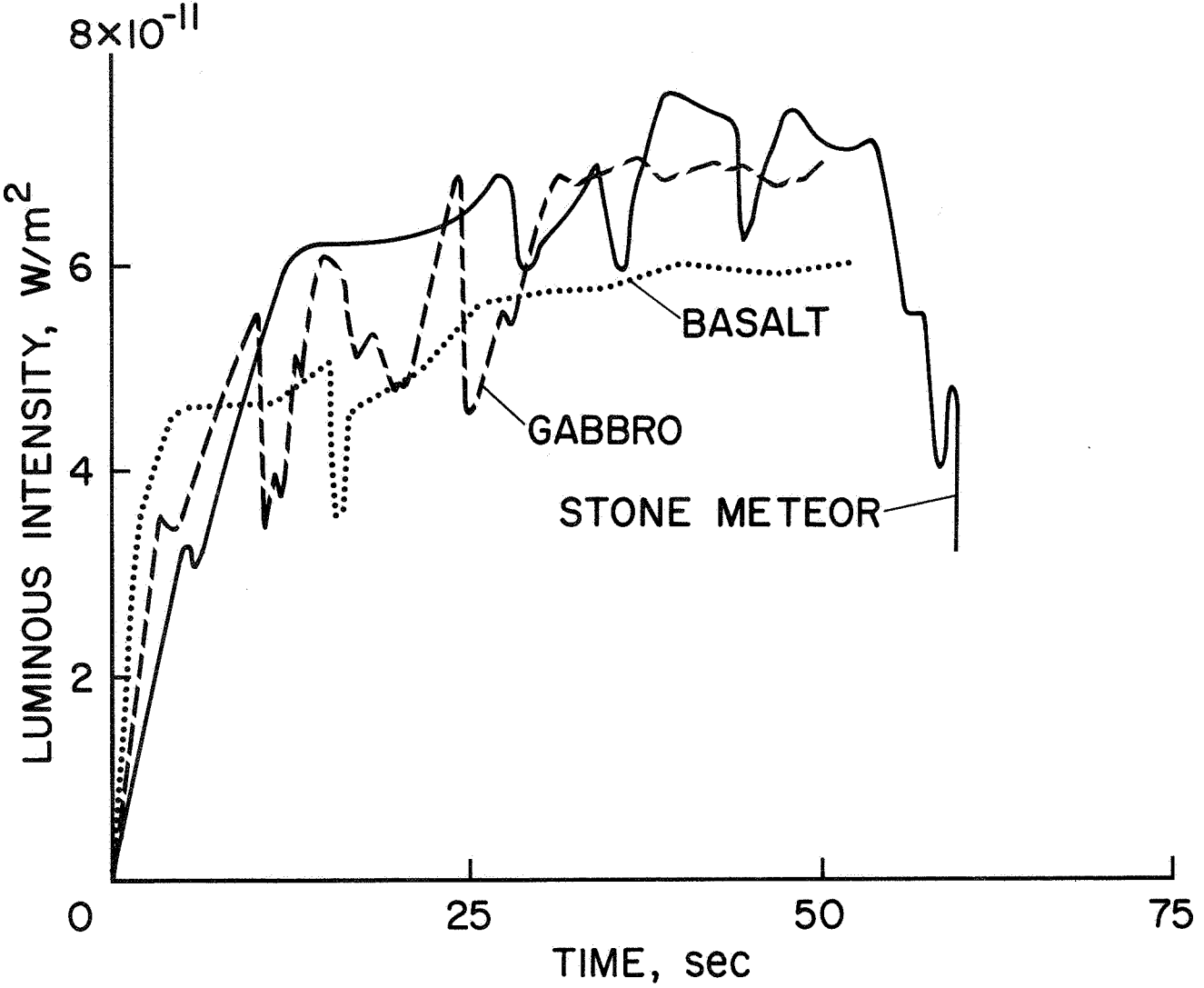

Fig. 15(a)

NATIONAL AERONAUTICS AND SPACE ADMINISTRATION
AMES RESEARCH CENTER, MOFFETT FIELD, CALIFORNIA

LUMINOUS INTENSITY NORMALIZED TO 100 km DISTANCE
COMPARISON OF STEEL AND IRON METEORITE MODELS
TEST CONDITION D

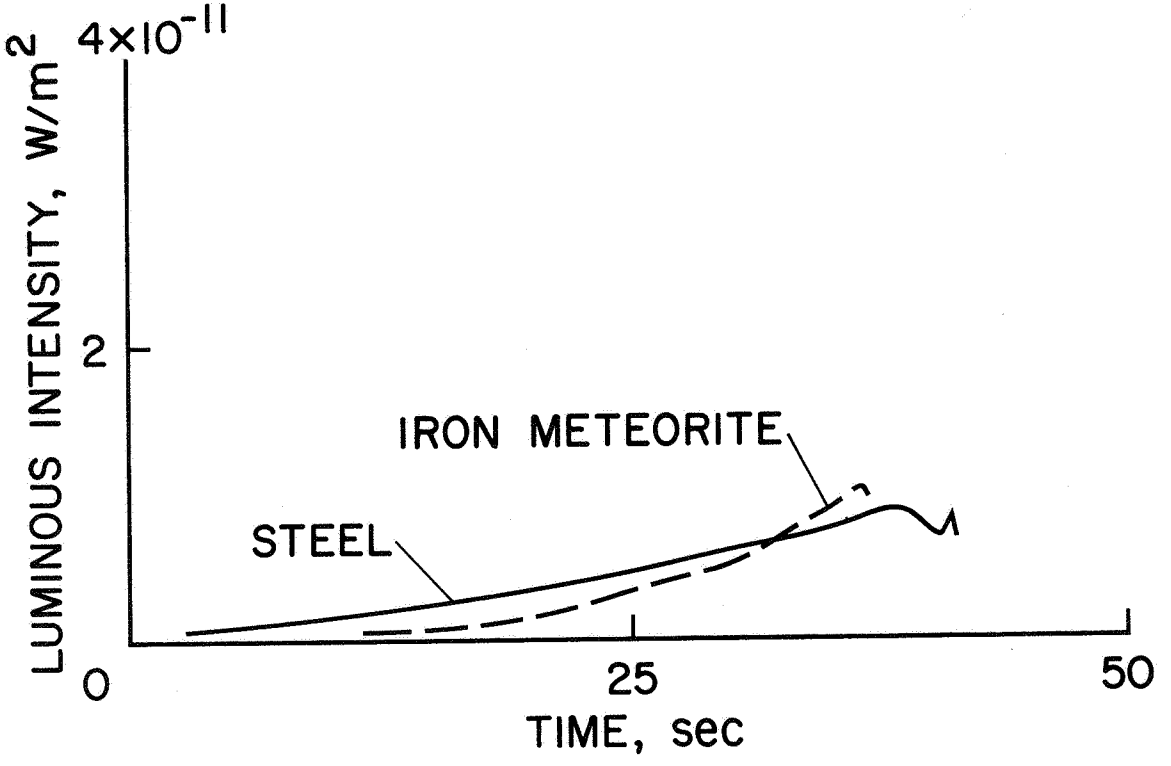

Fig. 15(b)

NATIONAL AERONAUTICS AND SPACE ADMINISTRATION
AMES RESEARCH CENTER, MOFFETT FIELD, CALIFORNIA

COMPARISON OF STEEL, BASALT AND JET FREE-STREAM RADIATION SPECTRA

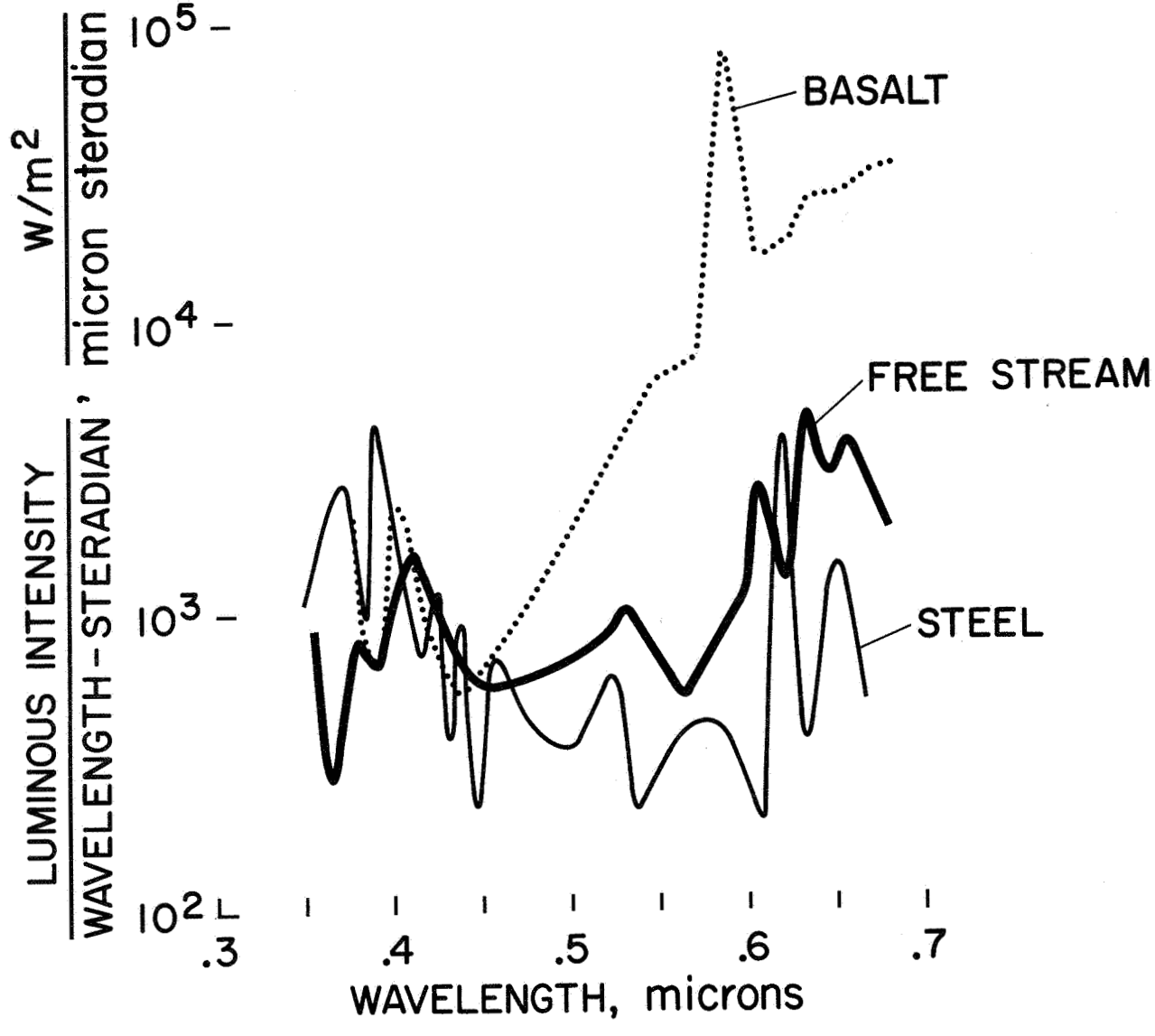

Fig. 16

NATIONAL AERONAUTICS AND SPACE ADMINISTRATION
AMES RESEARCH CENTER, MOFFETT FIELD, CALIFORNIA

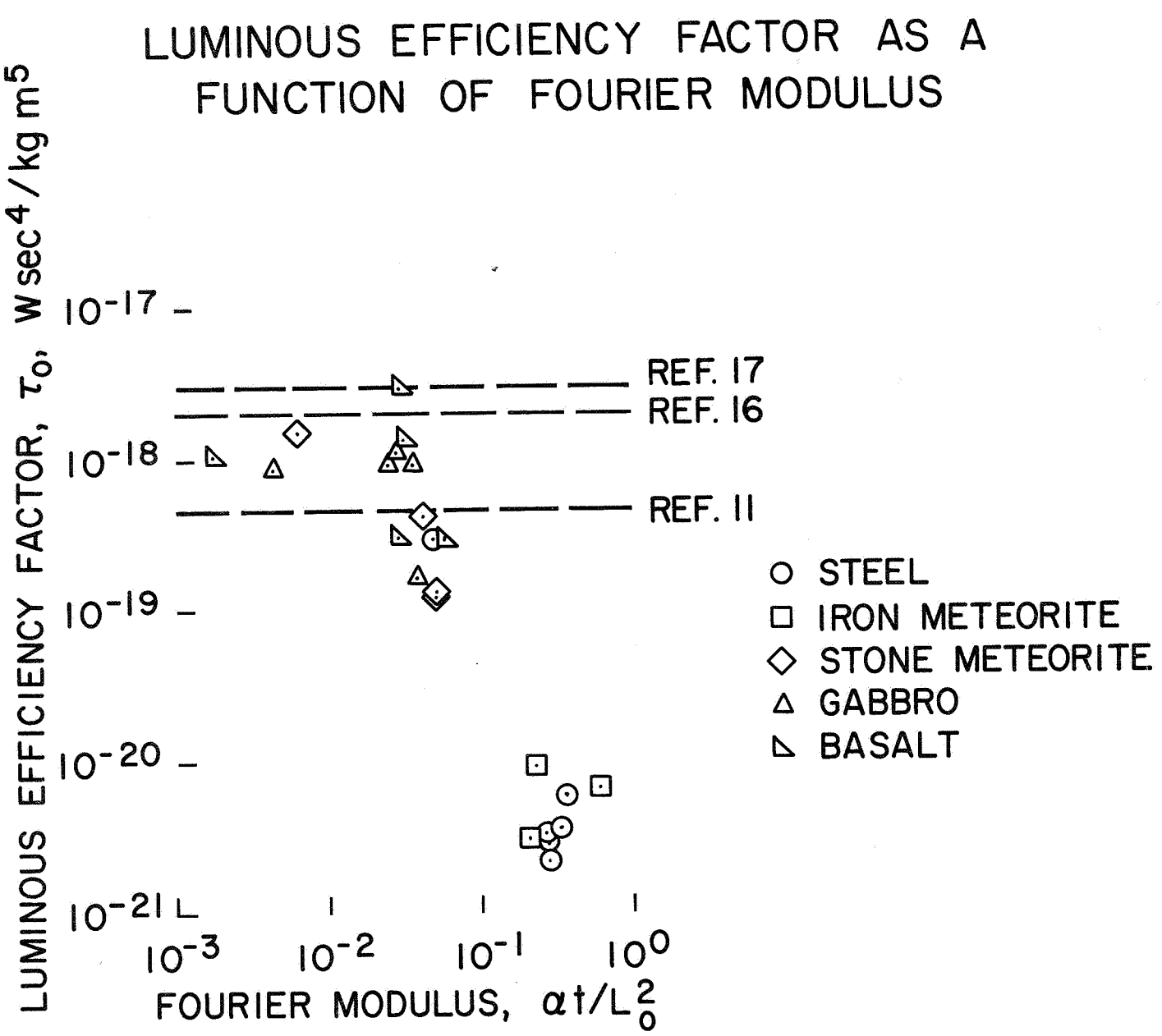

Fig. 17

NATIONAL AERONAUTICS AND SPACE ADMINISTRATION
AMES RESEARCH CENTER, MOFFETT FIELD, CALIFORNIA